LBNL-44119

ERNEST ORLANDO LAWRENCE
BERKELEY NATIONAL LABORATORY

Three-Dimensional Seismic Imaging of the Ryepatch Geothermal Reservoir

Mark A. Feighner, Roland Gritto, Thomas M. Daley,
Henk Keers, and Ernest L. Majer

Earth Sciences Division

November 1999

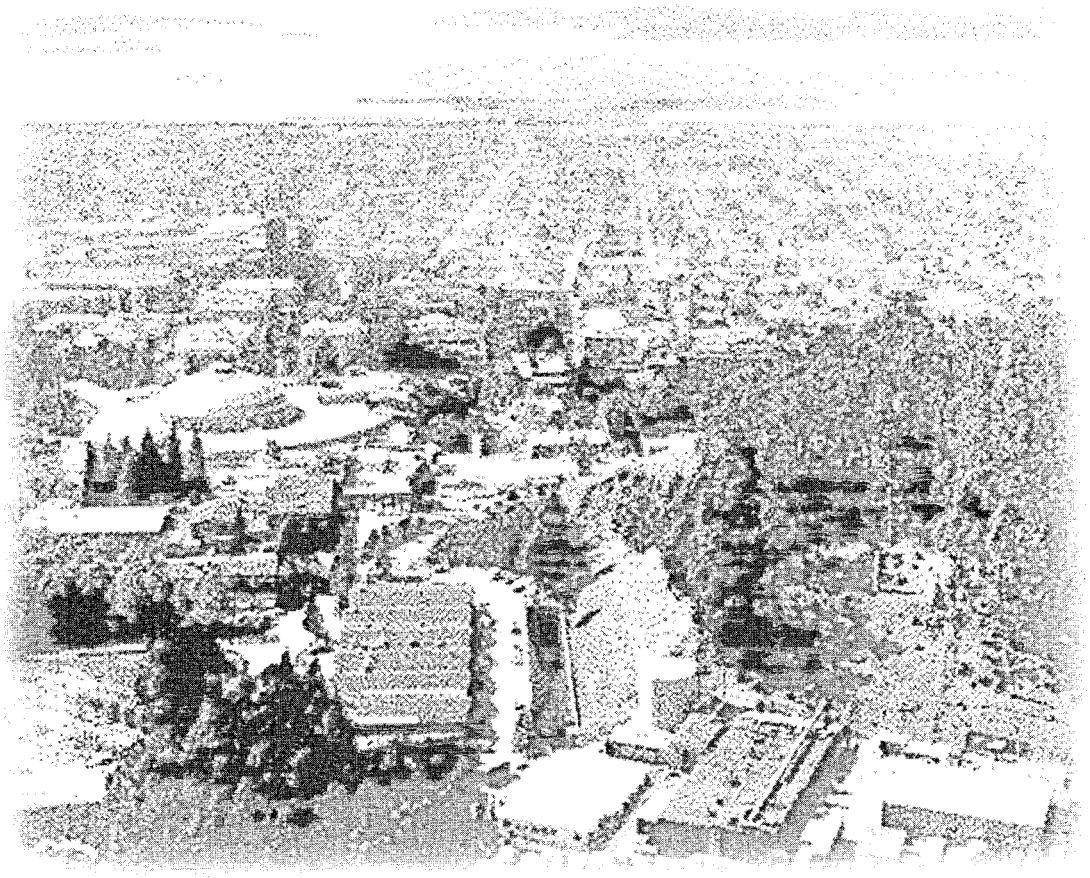

DISCLAIMER

LBNL-44119

Three-Dimensional Seismic Imaging of the Ryepatch Geothermal Reservoir

Mark A. Feighner[1], Roland Gritto[2], Thomas M. Daley[2],
Henk Keers[2,3], and Ernest L. Majer[2]

[1] *Department of Mathematics and Sciences, Solano Community College, Suisun, California*
[2] *Earth Sciences Division, Lawrence Berkeley National Laboratory, Berkeley, California*
[3] *Seismological Laboratory, University of California, Berkeley, California.*

November 1999

This research was supported by the Assistant Secretary for Energy Efficiency and Renewable Energy, Office of Geothermal and Wind Technologies of the US Department of Energy under contract No. DE-AC0376SF00098. Computations were carried out at the Center for Computational Seismology of the Lawrence Berkeley National Laboratory.

Three-Dimensional Seismic Imaging of the Rye Patch Geothermal Reservoir

Mark A. Feighner, Roland Gritto, Thomas M. Daley, Henk Keers and Ernest L. Majer
Earth Sciences Division, Lawrence Berkeley National Laboratory, Berkeley, CA

Abstract

A 3-D surface seismic survey was conducted to explore the structure of the Rye Patch geothermal reservoir (Nevada), to determine if modern seismic techniques could be successfully applied in geothermal environments. Furthermore, it was intended to map the structural features which may control geothermal production in the reservoir. The seismic survey covered an area of 3.03 square miles and was designed with 12 north-south receiver lines and 25 east-west source lines. The receiver group interval was 100 feet and the receiver line spacing was 800 feet. The source interval was 100 feet while the source line spacing was 400 feet. The sources were comprised of 4 vibrator trucks arranged in a box array. Seismic processing involved, among other steps, the picking of over 700,000 of the possible one million traces to determine first arrival travel times, normal moveout correction, 3-D stack, deconvolution, time migration, and depth conversion. The final data set represents a 3-D cube of the subsurface structure in the reservoir. Additionally, the travel times were used to perform tomographic inversions for velocity estimates to support the findings of the surface seismic imaging. The results suggest the presence of at least one dominant fault responsible for the migration of fluids in the reservoir. Furthermore, it is suggested that this feature might be part of a fault system that includes a graben structure.

1. Introduction

As part of the U.S. Department of Energy's (DOE) program in geothermal research Lawrence Berkeley National Laboratory (LBNL) has been cooperating with The Industrial Corporation (TIC) and Transpacific Geothermal Inc. (TGI) to evaluate and apply modern state-of-the-art seismic imaging methods for geothermal reservoir definition. The overall objective of the work was to determine if modern techniques in 3-D surface seismic profiling could be successfully applied in geothermal environments directly. If not, could they be modified to derive useful information on reservoir structure. Past efforts using 2-D seismic reflection have proved marginally successful in some cases but due to extreme heterogeneity in many geothermal areas 2-D seismic have not been cost effective.

Previous work by LBNL has shown that Vertical Seismic Poofiling (VSP) surveys can be very useful in Geothermal fields (*Daley et al.* [1988], *Majer et al.* [1988]). A VSP studies a relatively small volume of the reservoir in which the seismic response can be consistent despite larger scale heterogeneity in the reservoir. Surface seismic studies in geothermal fields have often been uninterpretable because of subsurface heterogeneity. However, one portion of the reservoir can be characterized with a VSP and the results interpolated away from the VSP well using surface seismic.

Initial exploration efforts at the Rye Patch, Nevada reservoir in the late 1980s and early 1990s resulted in one successful well (44-28), while other wells were either too cold or had no fluid flow. In 1997 TGI proposed a 3-D seismic survey to determine the geologic structure on the (hypothesized) fault-controlled reservoir. This would possibly be the first application of the 3-D seismic method to a geothermal field and therefore of interest to the entire geothermal community. Although the 3-D seismic method has proven an integral part of modern oil and gas exploration efforts the heterogeneous and hydrothermally altered nature of geothermal reservoirs makes all seismic imaging more difficult. It is not known how well the methods used in the petroleum industry can be transferred to the geothermal industry.

Before conducting a full-scale 3-D survey, DOE contracted LBNL to investigate the reflectivity of the target zone in order to assess the viability of seismic imaging in the Rye Patch area. In December 1997 LBNL obtained a VSP in well 46-28 to determine the seismic reflectivity in the area and to obtain velocity information for the design and potential processing of the proposed 3-D seismic survey *Feighner et al.* [1998]. Because the results of the VSP indicated apparent reflections, TGI proceeded with the collection of 3.0 square miles of 3-D surface seismic data over the Rye Patch reservoir. The data acquisition (which included the use of LBNL's three-component high temperature borehole geophone in well 44-28) was accomplished in August 1998. Initial processed results provided by the subcontractor Subsurface Exploration Co. (SECO) were delivered to TGI in December 1998.

After the initial analysis of SECO's results, it was decided that the processing was insufficient for correct analysis. LBNL was funded by DOE to reprocess the field data and asses the interpretability of the entire 3-D data set.

1.1. Project Objectives

The Rye Patch 3-D seismic project is intended to assess the applicability of 3-D seismic exploration techniques to geothermal reservoirs. The initial stage used a Vertical Seismic Profile to determine the seismic reflectivity of the Rye Patch area. The acquisition of the 3-D seismic data set is also intended to map the structural features which may control geothermal production in the Rye Patch reservoir.

2. Results From Vertical Seismic Profile (VSP)

Figure 1 shows the location of the Rye Patch geothermal field with Well 46-28 located within the marked Rye Patch Anomaly (*GeothermEx* [1997], from Figure 1.2). The VSP in Well 46-28 used a vibroseis source and a single-level, high temperature, hydraulic wall-locking, three-component seismometer. Data was acquired from 400 to 4200 ft depth using two-source offsets. The first break arrival times give a direct measure of the P-wave velocity with depth. The far-offset dataset was processed to image possible reflections at depth. Figure 2 shows the VSP data processed for reflected energy and shifted to the processing datum of the 3-D seismic data. The polarity has also been reversed to match that of the reflection data. The processing details are given in *Feighner et al.* [1998]. Two prominent, coherent reflectors can be seen at about 680 ms and 880 ms two-way travel time.

Figure 3 shows the VSP reflectors mapped at depth and superimposed onto a geologic cross sec-

tion (*GeothermEx* [1997]). This is the north-south cross section C-C' that intersects the VSP Well 46-28 in Figure 1. The upper reflector correlates with the sandstone/siltstone clastic unit of the Natchez Pass Formation. This is the main permeable clastic unit which supplies the thermal fluids to the Rye Patch wells. This reflection appears continuous for about 180 feet northwest of the well and then appears to truncate. The deeper reflector appears within the lower member of the Natchez Pass Formation and may occur at a limestone/siltstone interface.

In conclusion, the VSP data collected at Well 46-28 did produce a coherent reflection from the permeable clastic unit which is the main production unit in this geothermal field at a depth of about 3000 feet. Based on this result, it was decided to perform the 3-D seismic survey in order to map structure over a more extended region.

3. 3-D Seismic Imaging

3.1. Seismic Acquisition

The Rye Patch Geothermal Survey covered an area of 3.03 square miles and was designed with 12 north-south receiver lines and 25 east-west source lines (Figure 4). The receiver group interval was 100 feet and the receiver line spacing was 800 feet. The source interval was 100 feet while the source line spacing was 400 feet. There were 6 geophones per station in an in-line array. Four Litton 311 vibrators were used in a box array with the source flag at the center of the array. A detailed description of the data collection can be found in the contractor's report *SECO* [1998a]. Prior geologic knowledge of dip led to the array being shifted to the west to account for dip to the west in the subsurface.

3.2. Contractor Processing of the 3-D Seismic Data

The seismic data has been processed by two contractors: SECO of Pasadena, CA and Trend Technology (Trend Tech) of Midland, TX. Both companies provided LBNL with the final stack (in time and depth), the final migration (in time and depth) and the stacking velocities used in the processing. SECO also included three reports to LBNL: (1) A report outlining the permits, surveying, and data acquisition and processing (*SECO* [1998a]); (2) A binder with sample 2-D sections from their processed 3-D volumes (*SECO* [1998b]); and (3) A log describing the corrected field tapes that were sent to LBNL (*SECO* [1998c]). Trend Tech did not provide any support material.

A good way to compare processed 3-D volumes is to look at sample cross-sections. Figures 5a and 5b show a comparison of the final stack for the two contractor processed datasets as well as the results from LBNL's processing (covered in the next section). Figure 5a shows a W-E cross-section along inline number 43, which is at the location of the VSP Well 46-28 (see Figure 1). The well is located at crossline number 93. Figure 5b shows a N-S cross-section along crossline 93. In this figure, the VSP well is at inline number 43. Both the LBNL and Trend Tech datasets have applied a coherency filter after stack to enhance reflectors.

In Figure 5a, there is a west-dipping reflector near 680 ms two-way travel time on the LBNL and SECO sections. This matches the time from the VSP dataset for the clastic reflector. The geologic cross-sections from *GeothermEx* [1997] show a dip of 40 degrees or more for this clastic unit in this area. The Trend Tech section shows very little dip in the West-East direction and the events are highly coherent, even at large times. This would indicate that a large spatial smoothing was used in the coherency filter and that the range of allowable dips was limited. Because of this limitation, we believe the Trend Tech results are over processed and not usable for interpretation.

Figure 5b shows the comparison for the north-south crossline number 93. The dips in this direction are much less. The LBNL data shows some broken reflectors and produced the best overall stack.

3.3. LBNL Processing of the 3-D Seismic Data

SECO did the original processing of the 3-D seismic data. Because the data had already been processed, it was decided to give the data to LBNL with the geometry information incorporated into the trace headers. This avoided the time consuming process of assigning the field geometry to the trace headers. SECO also corrected some of the original field headers (*SECO* [1998c]) before giving the data to LBNL on two 8mm Exabyte tapes. It should be noted that errors in the trace header geometry could be present since LBNL did not assign the geometry headers independently; however, no obvious geometry errors where detected during our processing. The data traces were binned into CDP lines with 50 foot spacing. This resulted in 192 inlines (west-east direction) and 176 crosslines (south-north direction). The fold coverage is shown

in Figure 4.

LBNL tried to improve the quality of the reflection data by applying reflection and refraction statics to correct for lateral heterogeneity in the near-surface. However, neither static correction produced an improvement in the data for reasons that are outlined next.

In order to calculate refraction statics, the first break times must be picked for all the seismic traces. This is the arrival time of the first seismic energy on each trace (see Section 4 for a detailed description of the first break picking). The first break data were input into the refraction statics calculation program of ProMAX and a solution was obtained. However, the solution did not improve the reflection data, but rather degraded it. The reasons for this were twofold. First, offsets of less than about 2000 feet did not have impulsive first arrivals and were generally difficult to pick. Because of these many missing short-offsets picks, the obtained solution did not adequately sample the true variations in the near-surface velocity structure. Secondly, the velocity analysis of the VSP data (*Feighner et al.* [1998]) showed a velocity inversion near the bottom of the Tertiary section. This situation is referred to as a 'blind zone', since no first arrivals will be observed from this low-velocity zone. Even though good long-offset refraction arrivals were seen in the data, the calculated layer thicknesses based on the first arrival times would not have been correct. Although, the first break picks could not be used for refraction static corrections, these data were used for tomography studies that are covered in Section 4.

Next, the application of reflection statics was studied. In this method, a time window is chosen around a reflector in a Common Depth Point (CDP) gather, and the individual traces are time shifted before stack in an attempt to produce a more coherent reflection after stack. This method was unsuccessful for two reasons. First, the signal-to-noise ratio of the data was poor, which caused erroneous calculated time shifts. Second, the clastic unit was chosen as the reference reflector for the static shift, as it produced better reflections than other horizons; however, the reflection from this unit was spotty at best and appeared to be faulted in places. The statics program was not able to produce a solution that enhanced this reflection. Similarly, SECO and Trend Tech also were not able to obtain a statics solution that improved the quality of the reflection data. These shortcomings remain a problem in the 3-D data set.

The final processing flow is shown in Table 1. Field statics to smooth sudden changes in elevation were applied, followed by a bandpass filter and automatic gain control. Stacking velocities were picked for several horizons (Table 2) and Figure 6 shows a comparison between the three different datasets of the stacking velocities near the VSP Well 46-28. The estimated velocities from the VSP data are shown in black, while the other colors show the picks from the three processed datasets. LBNL's velocity estimates are closest to the VSP values, whereas SECO's and Trend Tech estimates were lower and higher, respectively. After normal moveout correction and 3-D Stack, a coherency filter was applied to the stacked data. This enhanced the strength of the weak reflectors. A bandpass filter and AGC were subsequently applied. This was followed by a time migration using smoothed stacking velocities that were shifted to the final datum of 4735 feet above sea level.

The time data was finally converted to depth using 103 percent of the VSP velocities listed in Table 3. These VSP velocities provided a match between the top of the clastic unit on the VSP and the center of the wavelet on the reflection data (Figure 7). In this figure, the VSP traces were stacked into one trace and repeated several times. The seismic response of the clastic unit can be seen as a blue-red-blue wavelet (negative-positive-negative). This corresponds to the same wavelet as in the reflection seismic data. The wavelength in the reflection data is longer, since the propagation distance from the surface to the reflector and back is greater such that higher frequencies (shorter wavelength) are stronger attenuated. Using the VSP velocities to convert from time to depth was appropriate at the well; however, the velocities certainly change with distance away from the well. Therefore, the calculated depths away from the well are only approximate and the uncertainty could easily approach several hundreds of feet. The only other alternative would have been to use a percentage of the stacking velocities. However, as shown in Figure 6, the stacking velocities would have been unreliable for depth conversion and we believe the resulting errors in depth would have been much greater than using the extrapolated VSP velocities. Additional VSP wells would have been useful in adding control to the depth conversion process and we would recommend this for future 3-D seismic surveys in geothermal areas.

3.4. Seismic Results

Because of the large volume of seismic data, only a few 2-D sections will be shown in this section. The inline and crossline migrated depth sections that cross three wells: 46-28, 44-28, and 42-28 are shown in Figures 8a, 8b, and 8c. Since the depth to geologic units are known in these wells, this information can be directly compared to the seismic data.

Figure 8a shows the two seismic lines that cross the VSP Well 46-28. Small 'x' symbols mark the location of geologic units within the well, labeled at the bottom of the figure. The clastic unit has the strongest reflection of any of the units. The center of the blue-red-blue wavelet corresponds to the top of the clastic unit. There appears to be significant westward dip and offset by faults in this section. The unit is more coherent on the eastern portion of the survey, while in the north-south direction it is more coherent to the south and appears faulted just north of the VSP Well.

The seismic data crossing the producing well 44-28 are shown in Figure 8b seem to generally be less coherent. The north-south Crossline 95 shows this very well, where the clastic unit was non-reflective in the center of the line. The seismic data near Well 42-28 (Figure 8c) shows the same pattern as for Well 44-28. It is important to notice that the blue-red-blue wavelet indicating most probably the top of the clastic unit does not correlate exactly with the geologic contact in these wells. This is due to the change in the velocity function at these locations and the mismatch gives an estimate of the amount of error in the depth conversion process.

In general, the clastic unit has poor reflectivity in the area of interest around the production well. The clastic unit was more coherent to the South and appeared to terminate just North of the VSP Well 46-28. This boundary is generally very distinct on many north-south crosslines and could be the location of the SE fault as indicated in the *GeothermEx* [1997] report. This fault has been interpreted from the seismic data and is shown in Figure 9 (Geothermex SE Fault) in conjunction with a second interpretation (SE Fault) (after Figure 7 by *Teplow* [1999]. The report by *Teplow* [1999] provides the interpretation of the data along with several other 2-D depth sections which can be seen in this report.

4. Seismic Tomography

4.1. Initial turning ray tomography

From the beginning of the project we believed that 3-D heterogeneity in the near surface and the subsurface due to tectonic activity and hydrothermal alteration would combine to reduce the effectiveness of standard 3-D seismic processing. Our desire to understand the near surface heterogeneity led us to attempt refraction and tomographic analysis using first arrival times. The arrival times represent a 3-D experiment independent of the CMP reflection processing, one which probes the shallow region of the reservoir.

Before analysis could begin the first arrival travel time data set had to be constructed. Standard industry practice is to use automatic time picking algorithms, such as neural network programs with "learning" ability. Our initial attempts at "automatic" time picking using industry standard software such as ProMAX were unsuccessful because of large lateral variation in travel time and waveform (see Figure 10). It is our experience in other heterogeneous subsurface environments that automatic time picking does not work because of the unpredictable changes in waveform and travel time caused by lateral variation in seismic velocity, attenuation or geologic structure. Because of the need for accurate travel times, we decided to hand pick all the seismic traces. Thus over 700,000 of the possible one million traces were picked. This effort was very time intensive (over 2 person-weeks), however the result was a consistent data set covering the 3-D volume.

Turning ray tomography represents an independent use of the travel times from the CMP reflection analysis. This large travel time data set was initially analyzed for tomographic images in the ProMAX package (also used for LBNL's CMP processing). The analysis used a turning ray tomography algorithm, one which assumes the rays penetrate to some depth and then turn back up to the surface. The penetration depth depends on the velocity structure. A positive velocity gradient is necessary to have turning rays. Turning ray tomography starts with computing the raypaths and the associated travel time for an initial velocity model and the source/receiver geometry of the field survey. The measured travel time (picked from the field data) which corresponds to each raypath is used in a tomographic inversion scheme to estimate one velocity which minimized the misfit between calculated and observed travel times.

For our initial test we chose receiver line number 7

(see Figure 11) because it crossed the VSP borehole and was near the center of the 3-D survey. Different velocity models were chosen for the raytracing because of problems to successfully trace far offset rays with models similar to the VSP survey. The most successful velocity model had a surface velocity of 8500 ft/s with a 10 ft/s per foot velocity gradient. This high gradient was used to capture the fast velocities (20,000 ft/s) seen below 2000 ft depth in the VSP. Four source points were used from each source line (2 west of Line number 7 and 2 east), giving a total of 9207 raypaths. The ray tracing found 8964 rays of the 9207 possible. Once the raypaths were computed for the starting model, a series of inversions were run varying the parameters to find the optimal result. Parameters varied included the horizontal and vertical smoothing, the damping factor (in number of rays), the maximum residual travel time to invert, and the minimum eigenvalue to invert. The best result was found with the following parameters: minimum eigenvalue to invert = 0.2; smoothing (horizontal and vertical) = 200 ft, damping factor = 30. This result (version 5.3) gave the velocity result shown in Figure 11. The most interesting structure of the inversion is the graben type feature between CDP 65 and 120. This result was found to spatially correspond to the changes in arrival time observed from the far offset source interpretation shown in section 5.1. The shallow velocities also show significant lateral variation along line 7, ranging between 3000 ft/s to over 10,000 ft/s in the top 500 ft. The deeper dipping structures on both sides below 1000 ft are artifacts of the ray coverage.

The results from this tomography were encouraging enough that we decided to proceed with 2-D travel time tomography on all 12 receiver lines, and thus build a 3-D tomographic data volume. This velocity data volume could be compared with the velocities derived from CMP analysis of reflections within the same 3-D volume. However, we did discover limitations of the turning ray algorithm in the ProMAX package. In particular, the actual locations of the raypath segments used in the inversion were not apparent to the user (because of binary encoded files). Furthermore the inversion algorithm was essentially a "black box", with limited user intervention. Because the tomography appeared promising, we desired a more controllable and open algorithm. We also hoped to work toward 3-D raytracing which would allow the use of all the picked travel times associated with rays that were not confined in the same plane. Therefore, the turning ray tomography was continued using LBNL in-house algorithms and software.

4.2. 2-D Raytracing and Travel Time Inversion

The original idea of a 3-dimensional data volume of estimated P wave velocities throughout the survey area had to be abandoned because of the nature of the survey geometry and the data acquisition process. While all 12 receiver lines had 87 or more receivers in north-south direction, there were only 12 receiver lines in east-west direction. This geometry prevents any reasonable resolution of inversion estimates in east-west direction. Furthermore, only the 4 nearest receiver lines in the immediate vicinity of the source locations recorded these shots. Therefore, only the lines in north-south direction were processed, and 2-dimensional ray tracing and travel time inversions were performed along these lines.

An initial velocity model which resembled the estimated velocity profile of the VSP survey was created. The surface velocity was chosen to be 7000 ft/s with a gradient of 125 ft/s per foot. Thus reaching values of 20000 ft/s at a depth of 5000 ft. In this model the velocity at 2000 ft depth is about 12000-13000 ft/s (see Figure 12a).

The 2-dimensional ray tracing algorithm is based on the shooting method. For each source position, rays are shot into the medium at various take-off angles, until one finds a path that reaches a receiver. For each ray the travel time for its propagation from source to receivers is determined. If more than one ray reaches a receiver, the shortest travel time determines the path that is associated with the first arriving energy. An example of the raytracing is given in Figure 12b. In this figure two sources are denoted by stars at the locations of receiver # 7095 and receiver # 7004, while 93 receivers are spread along the surface of the model indicated by triangles. The coverage of rays represents two fans of rays shot from each of the two sources to all receivers. It can be seen that the ray coverage above 1000 ft reveals a large number of crossing rays at various angles, while the coverage below 1500 ft shows mainly horizontal rays without many crossing paths. The crossing ray paths are an important feature in the inversion process which provides higher reliability for the velocity estimates, whereas poor ray coverage translates into less reliable inversion results.

The initial velocity model is subdivided into cells of constant velocity for the inversion process. The

cell size for this inversion is 100 ft in length and 50 ft in depth. The 2-dimensional inversion is based on backprojection. This methods subtracts the observed and calculated travel times, and transforms the travel time difference into a velocity anomaly according to the length of the associated raypath. The velocity anomaly is subsequently backprojected along the raypath and the starting velocity model is updated. In a second iteration, a new set of calculated travel times is determined based on the new velocity model, and the process of backprojection is repeated. This iterative process is performed until a predefined error between the observed and the calculated travel times is reached. The final result represents velocity estimates as a function of location in a 2-dimensional plane. The reliability of these estimates is qualitatively determined by counting the rays per cell. The more rays propagate through a cell, the more velocity values are backprojected into this cell, which makes the final estimate more reliable. Rays that cross the cell at many different angles carry more weight than rays that cross a cell parallel to each other. For this reason, the inversion results presented next are less reliable below a depth of 1500 ft.

Although inversions were done for all 12 receiver lines, reliable results were only obtained for two. As mentioned before, clear first arrival energy for intermediate distances was missing in the data of most lines. This lack of first arrival time picks transforms into poor ray coverage at intermediate depth. Since the ray coverage was always poor for depths below 1500 ft, the missing time picks limited reliable velocity estimates to the upper 500 ft. Therefore, only the results of receiver lines 7000 and 11000 will be shown.

The results for receiver line 7000 are shown in Figure 13. Only the colored areas indicate the inversion results, as the gray area is not covered by rays. The resolved area, however, shows continuous coverage with a minimum ray count of more than 20 rays per cell. The velocity estimates are presented in Figure 13a. The values between 1500 ft and 2000 ft depth increased, while they decreased in the shallow subsurface, relative to the starting model. During the inversion the relative residual between the calculated and observed travel times was reduced by a factor of 10, with the final maximum residual below 5%. The velocity estimated below 1500 ft depth increased to values of about 12500-13000 ft/s, which is in agreement with the estimates derived from the VSP survey, while the estimates for some near surface features decreased to values between 5000 ft/s and 6000 ft/s, possibly indicating the presence of sedimentary fill. The inversion process included static terms for source and receiver locations, such that local irregularities in the vicinity of these locations are not mapped into the velocity estimates. Therefore, we believe than the low estimates along the surface represent real velocity anomalies. At depth, a possible graben structure becomes evident between receiver # 7035 and # 7060 (3600 ft and 6200 ft distance). The throw appears to be about 200 ft at the southern end and 350 ft at the northern end with a base depth of about 600 ft. The ray coverage along the graben structure is good with a minimum of 40 rays per cell (Figure 13b). The geometry of the raypaths at this depth, with mainly horizontal and few vertical rays (see Figure 12b), suggests that the locations of the graben walls are better resolved than its depth.

The results of line 11 are presented in Figure 14 as they reveal an interesting correlation with the self potential (SP) and magnetic results, reported by *Teplow* [1999]. The depth image shows the overall problems with the lack of ray coverage. It is evident from Figure 14b that the ray coverage is not uniform revealing a gap in the central section. This gap is caused by the absence of first arrival energy for intermediate offsets, as discussed above. The lack of ray coverage transforms into an increase in variance of the velocity estimates. However, the shallow surface is well resolved and shows similar low velocity areas as Figure 13a. An interesting feature is the isolated velocity high (10000 ft/s) at receiver # 11048 (4800 ft distance) at a depth between 300 ft and 400 ft. This area is sufficiently resolved with a ray coverage of 25 - 30 rays per cell, such that it is possible to distinguish it from the lower surrounding velocity estimates. The location of this feature coincides with a low SP anomaly at N 2102826 and E 588408 and the intersection of two steep magnetic gradients, one trending NW and the other trending SSW as reported by *Teplow* [1999]. The velocity high could indicate an area of mineralization by fluids migrating upwards along the intersection of two non-resolved faults (Calcification), which tends to have higher velocity values than the surrounding material in this area.

5. Results From Other Seismic Datasets

5.1. Results From Four Far-Offset Shots

Four far-offset shots were collected when receiver lines 2 through 10 were active (Figure 15). The dis-

tances from the shots to the center of the receiver grid ranged between 3.4 and 4.2 miles. This resulted in a range in offsets of 2.5 to 5.3 miles for the active receivers. The purpose in collecting these data was to obtain far-offset refracted first arrival data that could be used to determine the deeper velocity structure.

The data quality varied significantly for each of the four shots indicating regional heterogeneity. The best datasets with the clearest arrival times were from shots 2 (northwest) and 4 (south). Figure 16 shows the data for Receiver Line 10 from Shot 4. The southern receivers recorded a sharp first arrival, but the signal abruptly disappears for the receivers towards the center of the array. This was a persistent pattern for the other receiver lines. Figure 15 shows the area where the first break arrivals were clearest. The central portion of the 3-D survey, including the area near the production Well 44-28, had weak or non-pickable arrivals. These boundaries may indicate the location of faults where seismic energy is attenuated and scattered resulting in no clear first arrival energy.

Shot 3 (west) had some arrivals on Receiver Lines 2 to 4, but were weak or absent on all the others. Shot 1 (north) had very weak or absent arrivals on nearly all the receivers.

6. Conclusions and Future Work

The 3-D seismic reflection data provided interpretable results for a depth range below 500 ft, whereas the tomographic travel time inversion produced reliable results down to 500 ft only.

The first notable result of the 3-D seismic processing is that neither refraction nor reflection static corrections helped to increase the data quality. The refraction static processing was unsuccessful because near offset first break arrivals were weak and could not be determined for most shots locations, whereas the target horizon for reflection statics (the clastic unit at depth) revealed incoherent reflections throughout the receivers lines, likely caused by faulting throughout the reservoir area. However, estimating correct surface statics could improve the CDP image.

The depth mapping of the time migrated data was based on velocity values equal to 103% of the VSP velocities. This approach lined up the reflection of the clastic unit in the VSP and reflection data at depth. However, these velocities are only valid in the vicinity of the VSP well, and have to be extrapolated at greater distance from the well. We still feel that this method is more exact than using stacking velocities, which are questionable due to the lack of horizontal continuity of the reflectors at depth.

The travel time tomography results indicate a possible graben structure along receiver line 7 (crossline 93), bound by two faults to the South and North. This interpretation is partially supported by the reflection seismic results, which indicate the presence of the southern fault of the hypothetic graben structure.

The inversion results along receiver line 11 indicate a velocity high between 300 ft and 400 ft depth which correlates with SP and magnetic results. The cause of this could be explained by an area of mineralization by fluids migrating upwards along the intersection of two non-resolved faults.

The lack of first arrival energy from the far offset shots in the shadow of the graben structure supports the tomography results as the graben faults may inhibit the waves on their propagation across this feature.

During the shooting of the 3-D seismic data, a 3-component seismometer was located at a depth of 3800 feet in the VSP Well 46-28 and recorded data from nearly all shots, including the 4 far-offset shots mentioned above. This data could be incorporated in future work to provide a better vertical resolution for tomographic travel time inversions.

Acknowledgments. We are grateful to Bill Teplow for his support in the interpretation of the seismic and tomographic data sets, and for his permission to use one of his figures in this report. This work was supported by the Assistant Secretary for Energy Efficiency and Renewable Energy, Office of Geothermal and Wind Technologies of the US Department of Energy under contract No. DE-AC03-76SF00098.

References

Daley, T.M., T.V. McEvilly and E.L. Majer, 1988, Analysis of P- and S-Wave vertical seismic profile data from the Salton Sea Scientific drilling project, *J. Geophys. Res., 93,B11,13025-13036.*

Feighner, M., Daley, T.M., Majer, E.L., 1998, Results of Vertical Seismic Profiling at Well 46-28, Rye Patch Geothermal Field, Pershing County, Nevada, *Lawrence Berkeley National Laboratory Report LBNL-41800.*

GeothermEx, 1997, Geology of the Rye Patch Geothermal Field, Pershing County, Nevada, *Internal Report, GeothermEx, Inc., Richmond, California.*

Majer, E. L., McEvilly T. V., Eastwood F., and Myer L., 1988, Fracture detection using P-wave and S-wave vertical seismic profiling at the Geysers, *Geophysics, 53, 76-84.*

SECO, 1998a, 3-D Seismic Survey, Rye Patch Geothermal Field, Pershing County, Nevada, June-August 1998, *Report, Subsurface Exploration Company, Pasadena, CA.*

SECO, 1998b, 3-D Seismic Survey, Rye Patch Geothermal Field, Pershing County, Nevada, June-August 1998, *2-D Sections, Subsurface Exploration Company, Pasadena, CA.*

SECO, 1998c, 3-D Seismic Survey, Rye Patch Geothermal Field, Pershing County, Nevada, June-August 1998, *Corrected Field Tape Log, Subsurface Exploration Company, Pasadena, CA, 23 pp.*

Teplow, B., 1999, Integrated Geophysical Exploration Program at the Rye Patch Geothermal Field, Pershing County, Nevada - Final Report.

M. A. Feighner, R. Gritto, T. M. Daley, H. Keers, E. L. Majer, Earth Sciences Division, Lawrence Berkeley National Laboratory, 1 Cyclotron Road, M.S. 90-1116, Berkeley, CA 94720 (mafeighner@lbl.gov, rgritto@lbl.gov, tmdaley@lbl.gov, hkeers@lbl.gov, elmajer@lbl.gov)

This preprint was prepared with AGU's LaTeX macros v4.
File report formatted November 22, 1999.

Table 1. LBNL Processing Flow

PROMAX PROCESSING STEP	PARAMETERS
SEG-Y Input	Sample Rate: 2 ms Trace Length: 2 sec
Extract Database Files	Apply Trace Headers to Geometry Database
Datum Statics Calculation	Final Datum Elev: 4735 feet Replacement Velocity: 6800 ft/s Length of Smoother: 15 CDP's
Datum Statics Apply	Apply Elevation Statics to Floating Datum
Bandpass Filter	10-80 Hz w/Notch Filter
Automatic Gain Control	Operator Length: 500 ms
Velocity Analysis	Pick Stacking Velocities (Listed in Table 2)
Normal Moveout Correction	Stretch Mute: 50 Percent
3D Stack	Shift to Final Datum
Disk Ouptut	Output: Final Stack Volume
F-XY Decon	Number of Inline Samples: 9 Number of Crossline Samples: 9 Length of Operator: 200 ms
Bandpass Filter	10-80 Hz
Automatic Gain Control	Operator Length: 500 ms
Disk Ouptut	Output: F-XY Decon Volume
Kirchhoff Time Migration	Maximum Dip to Migrate: 75 Degrees Velocity Model: Smoothed Stacking Velocities Shifted to Final Datum
Disk Ouptut	Output: Final Migrated Time Volume
Time/Depth Conversion	Used 103% of VSP Velocities at Final Datum (Listed in Table 3)
Disk Ouptut	Output: Final Migrated Depth Volume

Table 2. Stacking Velocities

X COOR (ft)	Y COOR (ft)	CDP	TIME (ms)	VEL (ft/s)
581765.1	2100634.2	5296.0	24.3	4403.5
			156.0	5349.7
			446.3	8125.2
			651.2	10837.7
			1143.9	12730.1
			1531.8	16136.4
			1887.9	17208.7
581807.8	2101383.0	7936.0	36.5	4727.6
			132.0	4905.8
			580.6	7935.6
			892.0	10133.6
			1361.3	13579.3

Table 2. (continued)

X COOR (ft)	Y COOR (ft)	CDP	TIME (ms)	VEL (ft/s)
			1706.0	15836.7
			1876.3	16193.2
581850.4	2102132.0	10576.0	24.1	4252.3
			248.3	5856.3
			663.6	8945.5
			867.1	10133.6
			1000.0	10965.3
			1078.9	12391.1
			1560.6	15955.5
			1730.9	16252.6
581893.1	2102880.8	13216.0	32.4	4371.1
			198.5	5440.5
			393.7	6866.2
			829.7	10490.1
			1228.4	13341.6
			1573.1	15242.7
			1938.6	15480.3
582855.1	2106582.0	26431.0	36.5	4252.3
			127.9	4489.9
			456.0	6806.8
			838.0	9896.0
			1216.0	12628.7
			1568.9	15123.8
			1876.3	15480.3
582897.7	2107330.8	29071.0	3.3	3955.3
			211.0	4965.2
			514.1	7460.3
			829.7	9955.4
			1203.5	12688.1
			1431.9	14826.8
			1863.8	16430.8
582940.4	2108079.8	31711.0	32.4	4074.1
			364.6	6450.4
			809.0	8886.1
			987.5	11559.4
			1577.3	15123.8
			1838.9	16371.4
583305.3	2101297.8	7966.0	19.9	5262.2
			285.7	6906.3
			800.7	11618.8
			1382.1	14886.2

Table 2. (continued)

X COOR (ft)	Y COOR (ft)	CDP	TIME (ms)	VEL (ft/s)
			1660.3	16252.6
			1884.6	16430.8
584096.8	2102004.2	10621.0	53.1	4787.0
			285.7	6569.2
			543.2	9420.7
			1137.0	13282.2
			1610.5	16609.0
584267.3	2104999.2	21181.0	28.2	5262.2
			256.6	6509.8
			456.0	9717.8
			850.5	12450.5
			1265.8	14529.8
			1622.9	16609.0
584760.2	2100463.8	5356.0	36.5	5024.6
			132.0	5262.2
			306.5	7103.9
			489.2	9183.1
			854.6	12450.5
			1415.3	15480.3
			1905.3	16193.2
585144.1	2107202.8	29116.0	32.4	5084.0
			269.1	6866.2
			597.2	10371.3
			908.6	12925.8
			1315.6	15005.0
			1652.0	16549.6
585186.8	2107951.8	31756.0	28.2	4549.3
			343.8	7222.7
			638.7	11813.6
			1232.6	14945.6
			1622.9	17321.9
585426.5	2098973.8	267.0	19.4	5143.4
			121.8	5856.3
			273.1	6806.8
			512.1	10348.8
			926.8	12509.9
			1346.4	14886.2
			1939.1	16787.3
585466.3	2099672.5	2731.0	280.4	6153.3
			604.8	11004.0
			1283.0	14113.9

Table 2. (continued)

X COOR (ft)	Y COOR (ft)	CDP	TIME (ms)	VEL (ft/s)
			1636.7	16846.7
			1946.5	16490.2
585509.0	2100421.2	5371.0	24.1	4846.4
			132.0	5202.8
			331.4	6925.6
			497.5	9123.7
			634.5	10727.7
			1153.7	13876.3
			1614.6	16965.5
585551.6	2101170.0	8011.0	15.8	5381.0
			360.5	7282.1
			568.1	10608.9
			1016.6	14232.7
			1535.7	15717.9
			1814.0	16727.8
585764.9	2104914.0	21211.0	32.4	5084.0
			248.3	6747.4
			489.2	9717.8
			572.3	12569.3
			1099.7	14411.0
			1498.3	16965.5
			1797.4	17262.5
585807.5	2105662.8	23851.0	32.4	5024.6
			273.2	6628.6
			613.8	11975.3
			1157.8	14589.2
			1539.9	16430.8
			1917.8	16430.8
586300.4	2101127.2	8026.0	28.2	5084.0
			298.2	6985.0
			543.2	10133.6
			883.7	12391.1
			1328.1	14411.0
			1664.5	16787.3
			1838.9	16906.1
588461.4	2099501.8	2791.0	21.1	4965.2
			177.7	5856.3
			386.6	7341.5
			512.7	8886.1
			852.1	12688.1
			1013.1	12747.6

Table 2. (continued)

X COOR (ft)	Y COOR (ft)	CDP	TIME (ms)	VEL (ft/s)
			1339.4	15005.0
			1670.0	16668.4
588546.8	2100999.2	8071.0	11.6	4668.2
			227.6	6509.8
			480.9	9420.7
			755.0	11084.1
			1174.4	13282.2
			1544.0	16015.0
			1988.4	16490.2

Table 3. VSP RMS Velocities at Final Datum

X COOR (ft)	Y COOR (ft)	CDP	TIME (ms)	VEL (ft/s)
585643.0	2101014.5	7485.0	92.5	6800.0
			102.5	6800.7
			112.5	6801.5
			122.5	6802.2
			132.5	6802.9
			142.5	6803.7
			152.5	6804.4
			162.5	6805.1
			172.5	6805.9
			182.5	6806.6
			192.5	6807.3
			202.5	6810.5
			212.5	6945.1
			222.5	7309.5
			232.5	7598.3
			242.5	7767.1
			252.5	7884.4
			262.5	7953.8
			272.5	8083.9
			282.5	8281.3
			292.5	8408.8
			302.5	8466.8
			312.5	8655.0
			322.5	8903.9
			332.5	8957.5
			342.5	8966.4
			352.5	8991.1
			362.5	9004.8
			372.5	8992.0
			382.5	8962.6

Table 3. (continued)

X COOR (ft)	Y COOR (ft)	CDP	TIME (ms)	VEL (ft/s)
			392.5	8948.2
			402.5	8931.8
			412.5	8904.0
			422.5	8866.0
			432.5	8818.5
			442.5	8778.0
			452.5	8753.5
			462.5	8757.1
			472.5	8755.9
			482.5	8741.0
			492.5	8737.7
			502.5	8746.6
			512.5	8743.7
			522.5	8722.7
			532.5	8704.1
			542.5	8698.9
			552.5	8682.0
			562.5	8671.8
			572.5	8732.4
			582.5	8851.5
			592.5	9081.5
			602.5	9379.8
			612.5	9739.9
			622.5	10086.1
			632.5	10405.9
			642.5	10674.2
			652.5	10846.0
			662.5	11062.7
			672.5	11190.7
			682.5	11346.6
			692.5	11505.8
			702.5	11757.9
			712.5	12010.2
			722.5	12299.2
			732.5	12525.2
			742.5	12658.6
			752.5	12828.0
			762.5	12952.9
			772.5	13070.2
			782.5	13160.4
			792.5	13206.3

Table 3. (continued)

X COOR (ft)	Y COOR (ft)	CDP	TIME (ms)	VEL (ft/s)
			802.5	13358.5
			812.5	13399.0
			822.5	13420.5
			832.5	13442.0
			842.5	13463.4
			852.5	13484.9
			862.5	13506.4
			872.5	13527.8
			882.5	13549.3
			892.5	13570.7
			902.5	13592.2
			912.5	13613.7
			922.5	13635.1
			932.5	13656.6
			942.5	13678.1
			952.5	13699.5
			962.5	13721.0
			972.5	13742.4
			982.5	13763.9
			992.5	13785.4
			1002.5	13806.8
			1012.5	13828.3
			1022.5	13849.8
			1032.5	13871.2
			1042.5	13892.7
			1052.5	13914.2
			1062.5	13935.6
			1072.5	13957.1
			1082.5	13978.5
			1092.5	13999.7
			1102.5	14020.0
			1112.5	14040.0
			1122.5	14060.0
			1132.5	14080.0
			1142.5	14100.0
			1152.5	14120.0
			1162.5	14140.0
			1172.5	14160.0
			1182.5	14180.0
			1192.5	14200.0
			1202.5	14220.0

Table 3. (continued)

X COOR (ft)	Y COOR (ft)	CDP	TIME (ms)	VEL (ft/s)
			1212.5	14240.0
			1222.5	14260.0
			1232.5	14280.0
			1242.5	14300.0
			1252.5	14320.0
			1262.5	14340.0
			1272.5	14360.0
			1282.5	14380.0
			1292.5	14400.0
			1302.5	14420.0
			1312.5	14440.0
			1322.5	14460.0
			1332.5	14480.0
			1342.5	14500.0
			1352.5	14520.0
			1362.5	14540.0
			1372.5	14560.0
			1382.5	14580.0
			1392.5	14600.0
			1402.5	14620.0
			1412.5	14640.0
			1422.5	14660.0
			1432.5	14680.0
			1442.5	14700.0
			1452.5	14720.0
			1462.5	14740.0
			1472.5	14760.0
			1482.5	14780.0
			1492.5	14800.0
			1502.5	14820.0
			1512.5	14840.0
			1522.5	14860.0
			1532.5	14880.0
			1542.5	14900.0
			1552.5	14920.0
			1562.5	14940.0
			1572.5	14960.0
			1582.5	14980.0
			1592.5	15003.6
			1602.5	15040.0
			1612.5	15080.0

Table 3. (continued)

X COOR (ft)	Y COOR (ft)	CDP	TIME (ms)	VEL (ft/s)
			1622.5	15120.0
			1632.5	15160.0
			1642.5	15200.0
			1652.5	15240.0
			1662.5	15280.0
			1672.5	15320.0
			1682.5	15360.0
			1692.5	15400.0
			1702.5	15440.0
			1712.5	15480.0
			1722.5	15520.0
			1732.5	15560.0
			1742.5	15600.0
			1752.5	15640.0
			1762.5	15680.0
			1772.5	15720.0
			1782.5	15760.0
			1792.5	15800.0
			1802.5	15840.0
			1812.5	15880.0
			1822.5	15920.0
			1832.5	15960.0
			1842.5	15996.4
			1852.5	16020.0
			1862.5	16040.0
			1872.5	16060.0
			1882.5	16080.0
			1892.5	16100.0
			1902.5	16120.0
			1912.5	16140.0
			1922.5	16160.0
			1932.5	16180.0
			1942.5	16200.0
			1952.5	16220.0
			1962.5	16240.0
			1972.5	16260.0
			1982.5	16280.0
			1992.5	16300.0
			2002.5	16320.0

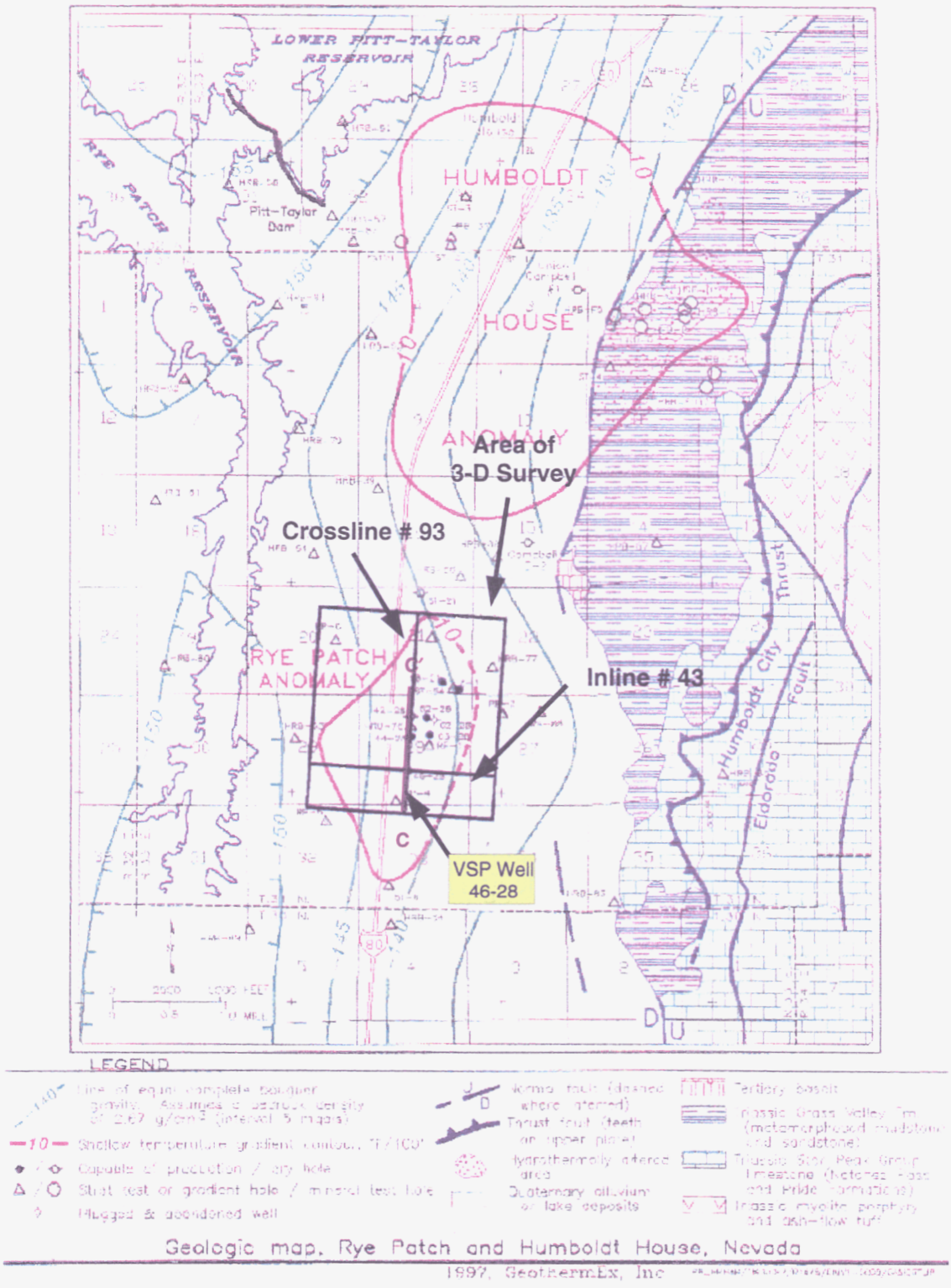

Figure 1. Location map with area of 3-D survey. Also shown are the cross-section profiles of C-C', Inline 43, and Crossline 93. All these cross-sections pass near the VSP Well 46-28.

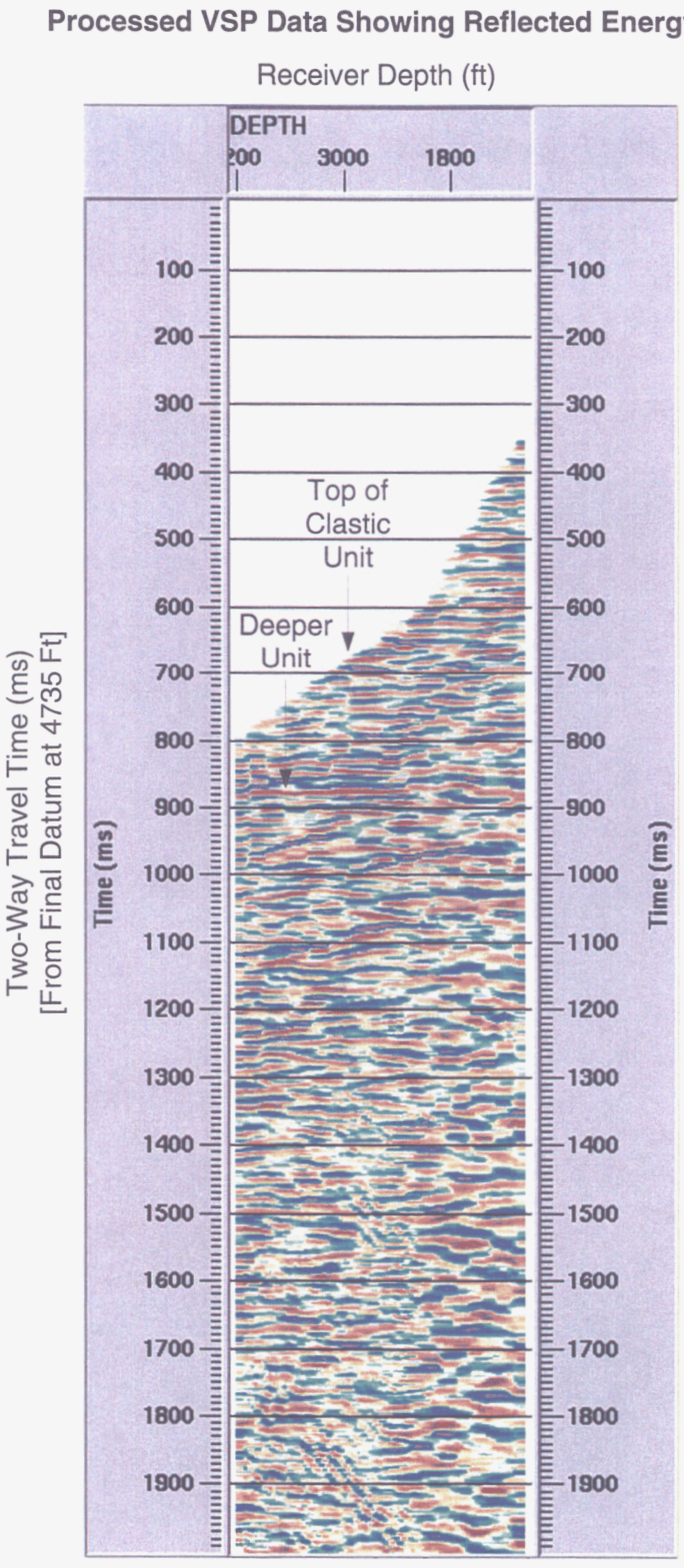

Figure 2. Reflected energy from the VSP data in two-way travel time. Two coherent reflectors can be seen, including the clastic unit of interest.

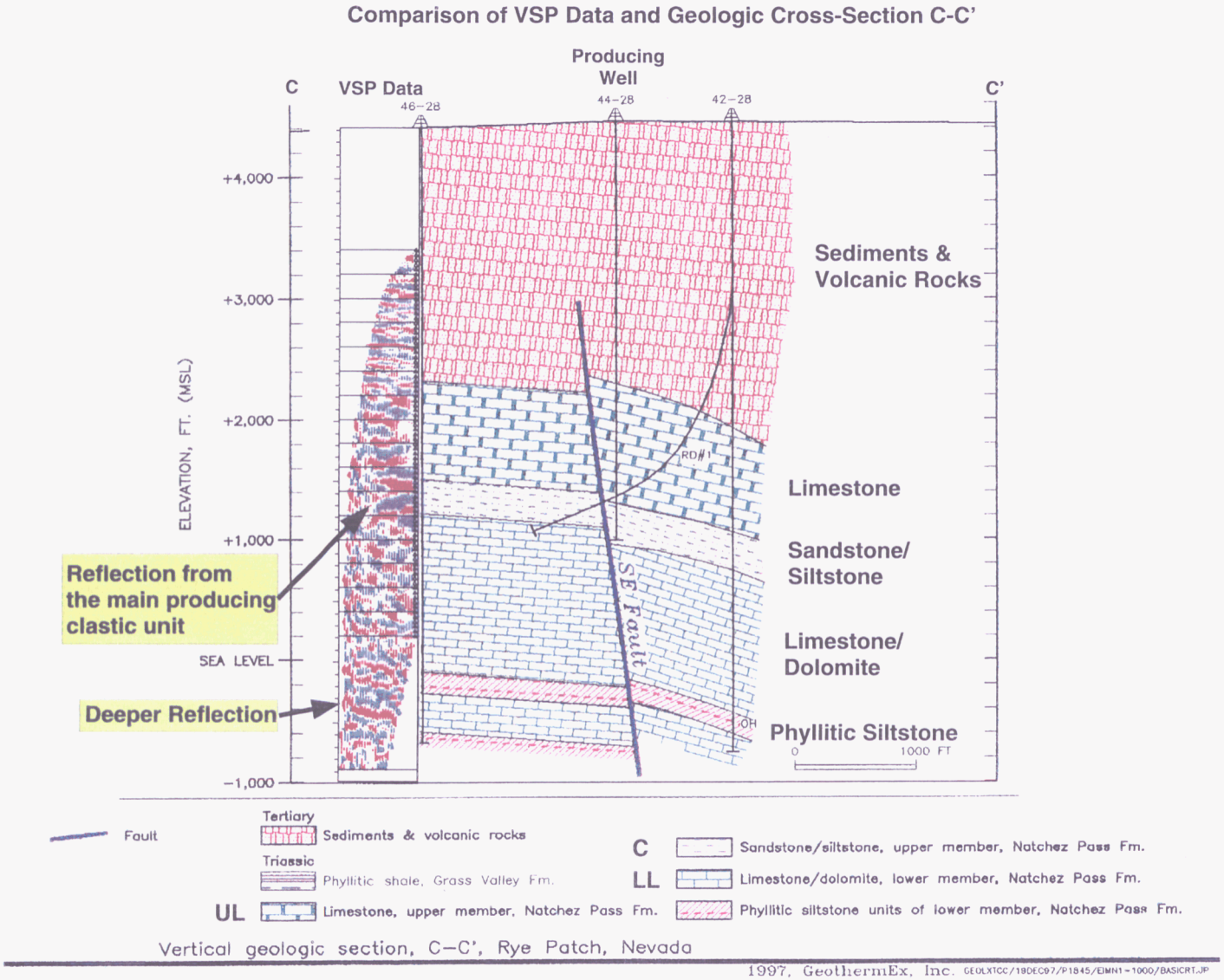

Figure 3. VSP data converted to depth with comparison to geologic cross-section C-C' (see Figure 1).

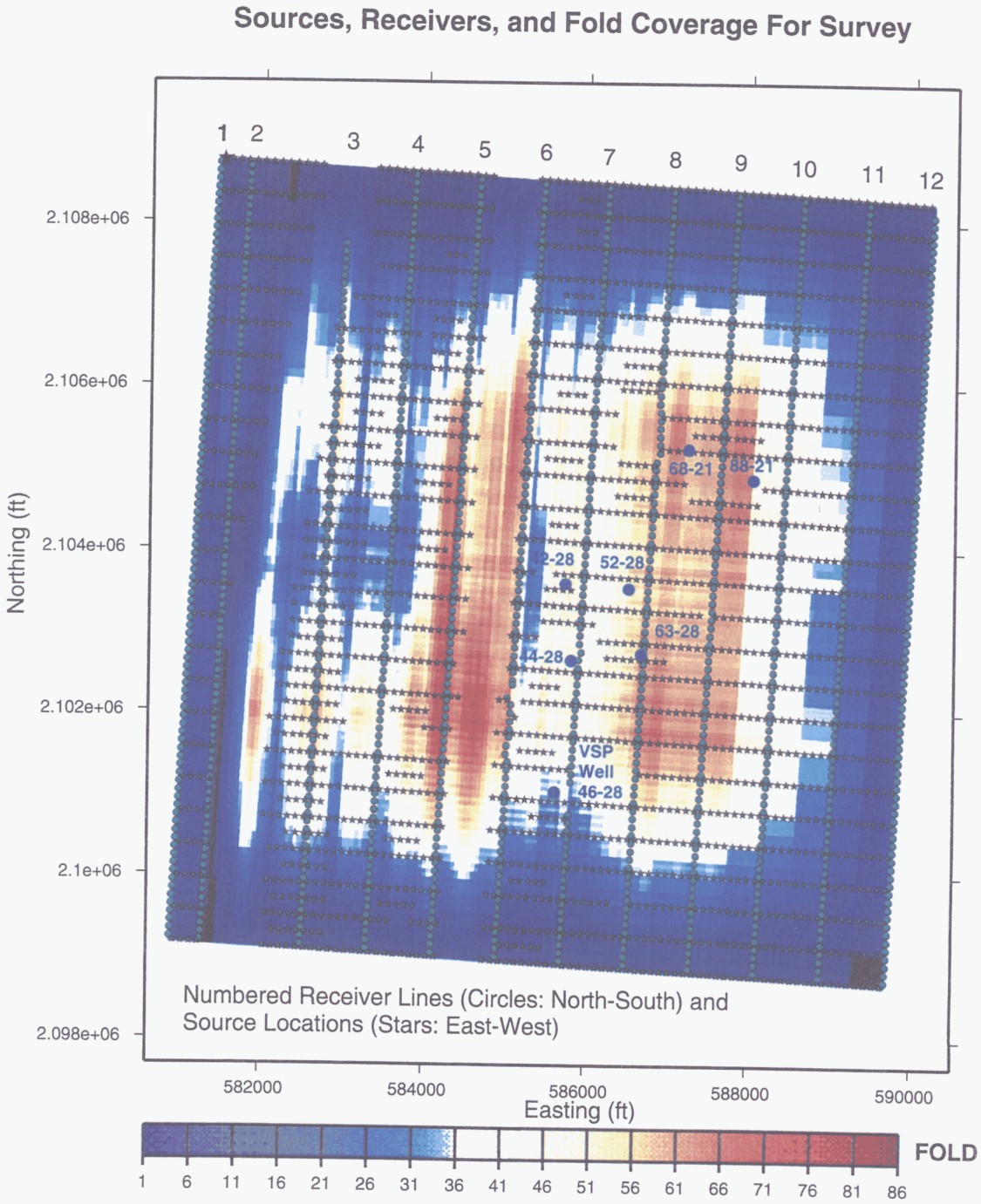

Figure 4. Fold coverage map with location of receivers, sources, and wells.

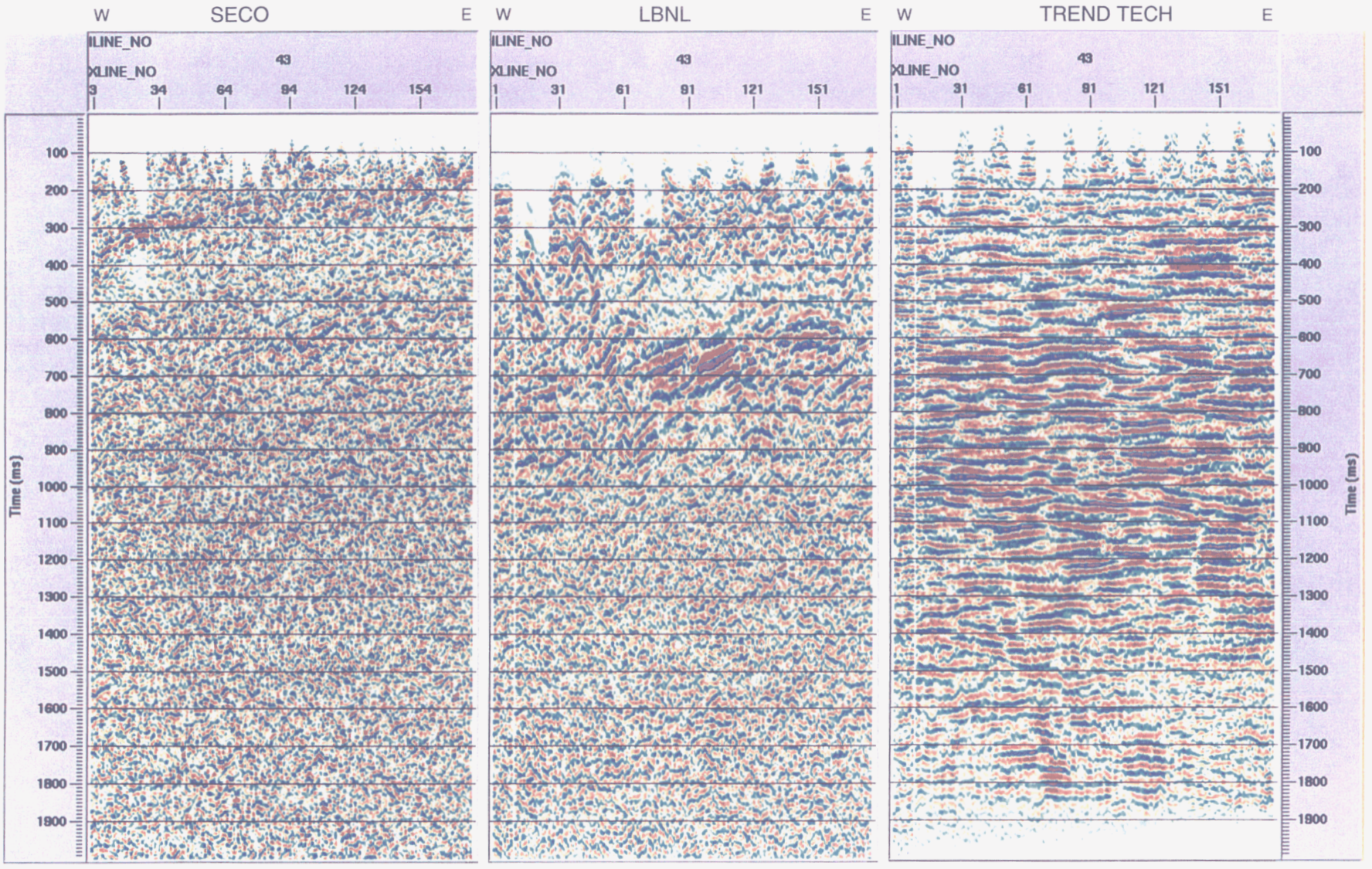

Figure 5a. Comparison of processed seismic data along Inline 43 (see Figure 1).

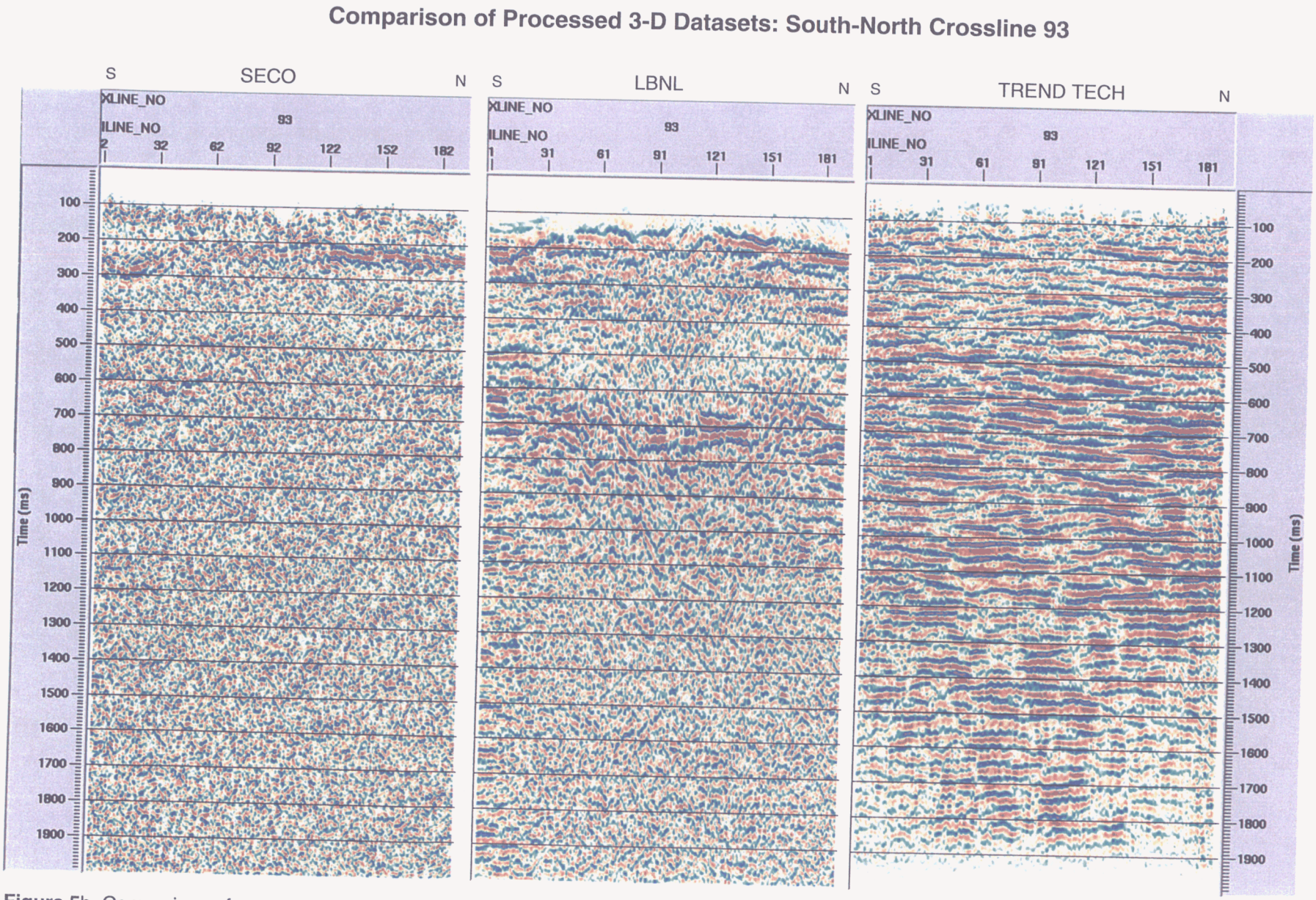

Figure 5b. Comparison of processed seismic data along Crossline 93 (see Figure 1).

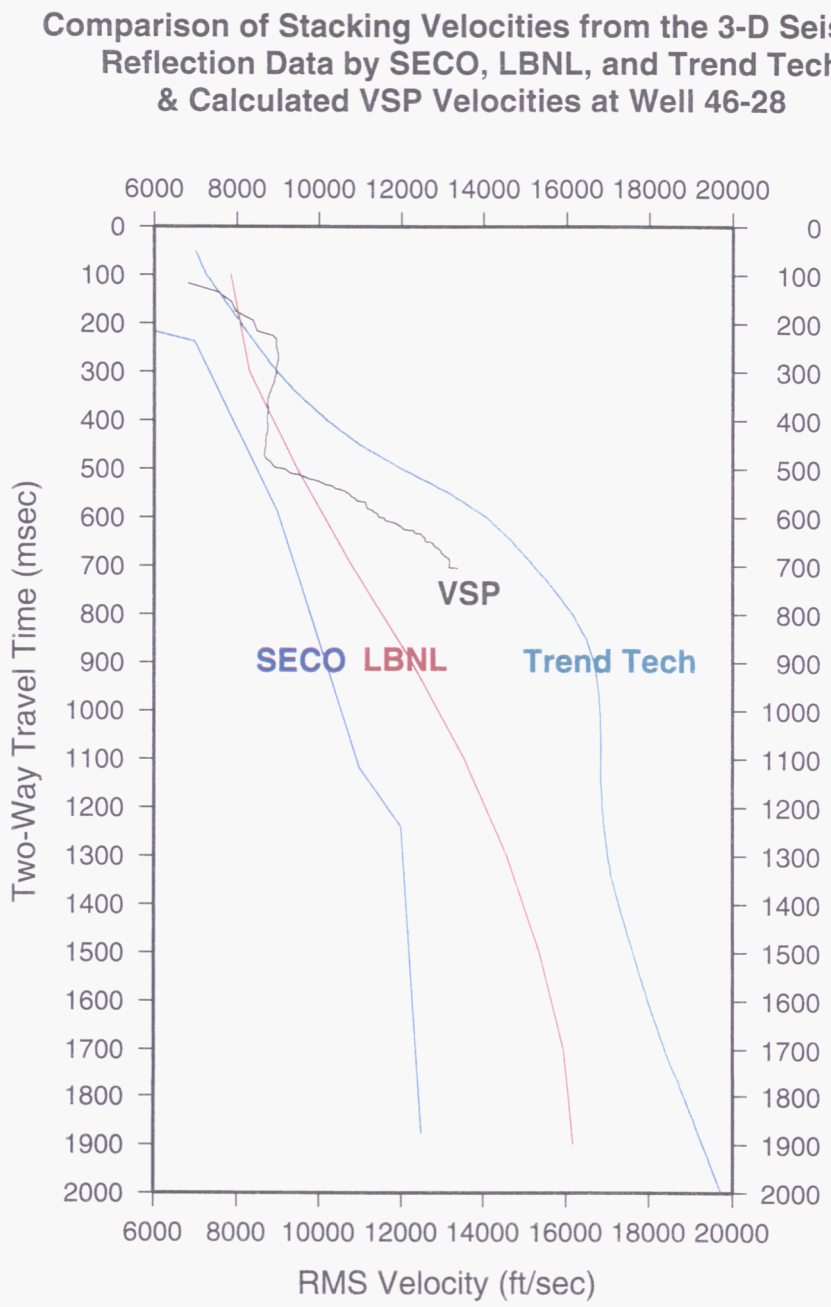

Figure 6. Comparison of stacking velocities near the VSP Well 46-28.

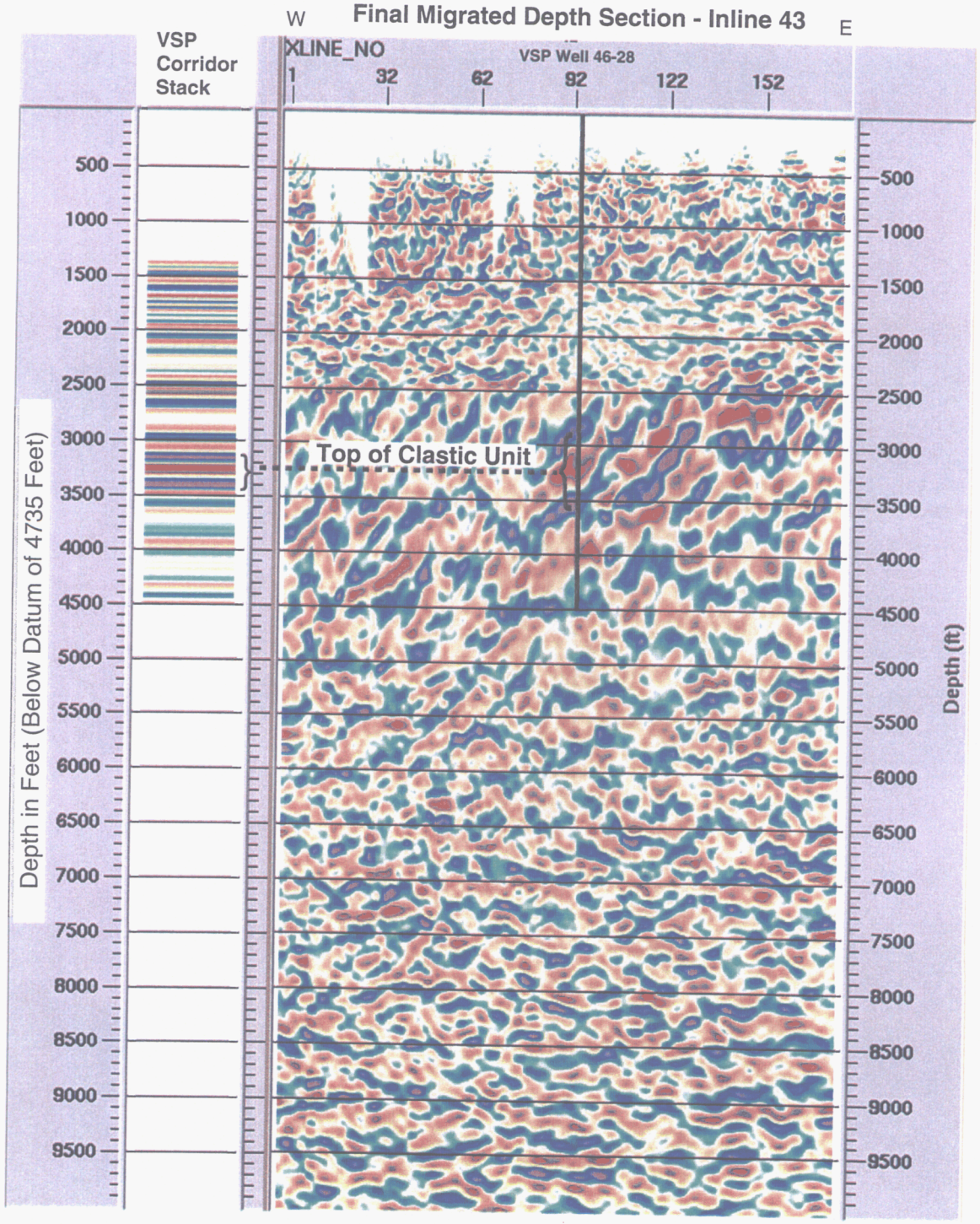

Figure 7. Comparison of a corridor stack of the VSP data from Well 46-28 and the final migrated depth section along Inline 43.

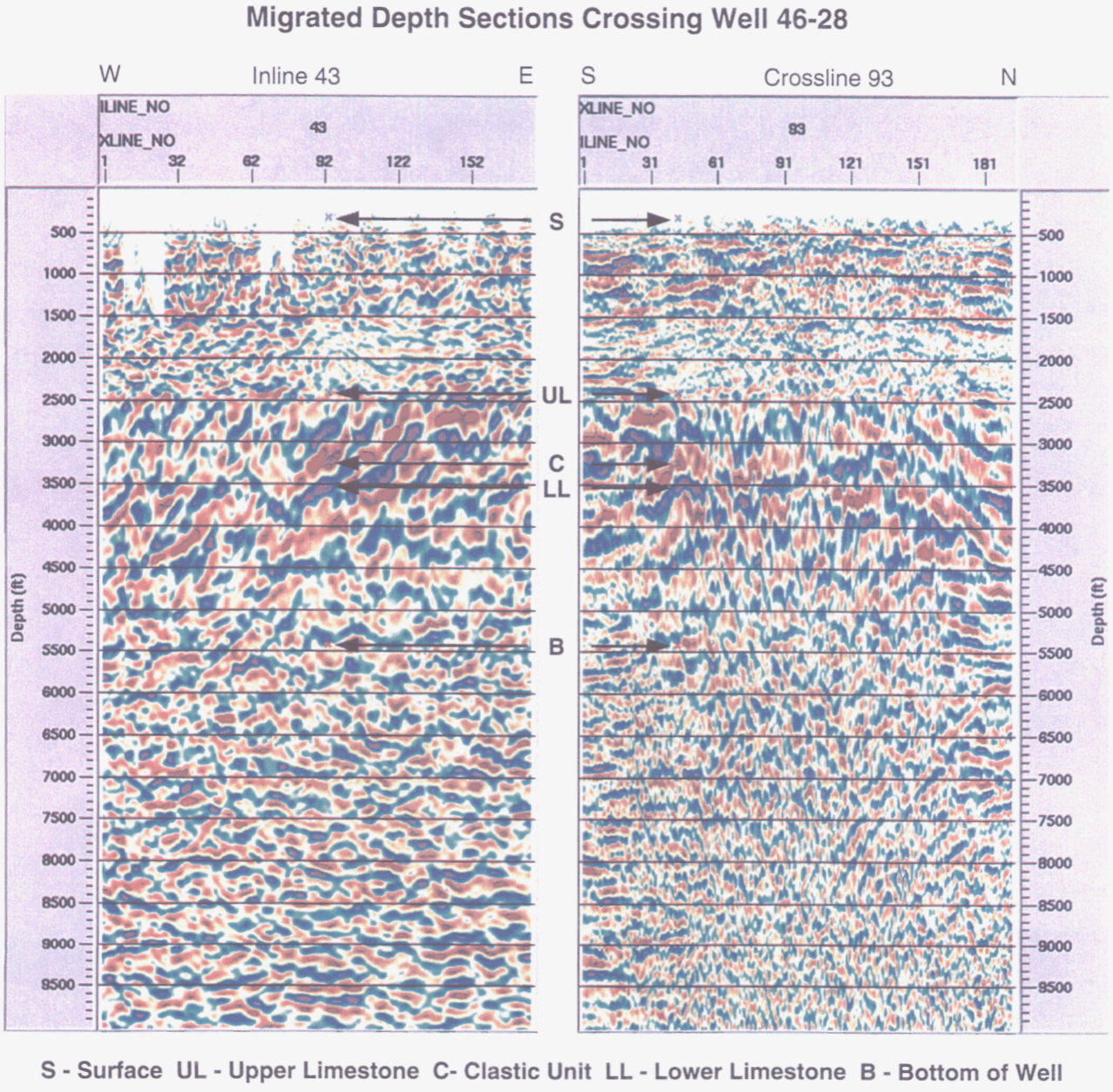

Figure 8a. Shown here are the two final migrated depth sections that cross the VSP Well 46-28. The total depth of the well is marked along with important geologic contacts shown in Figure 3.

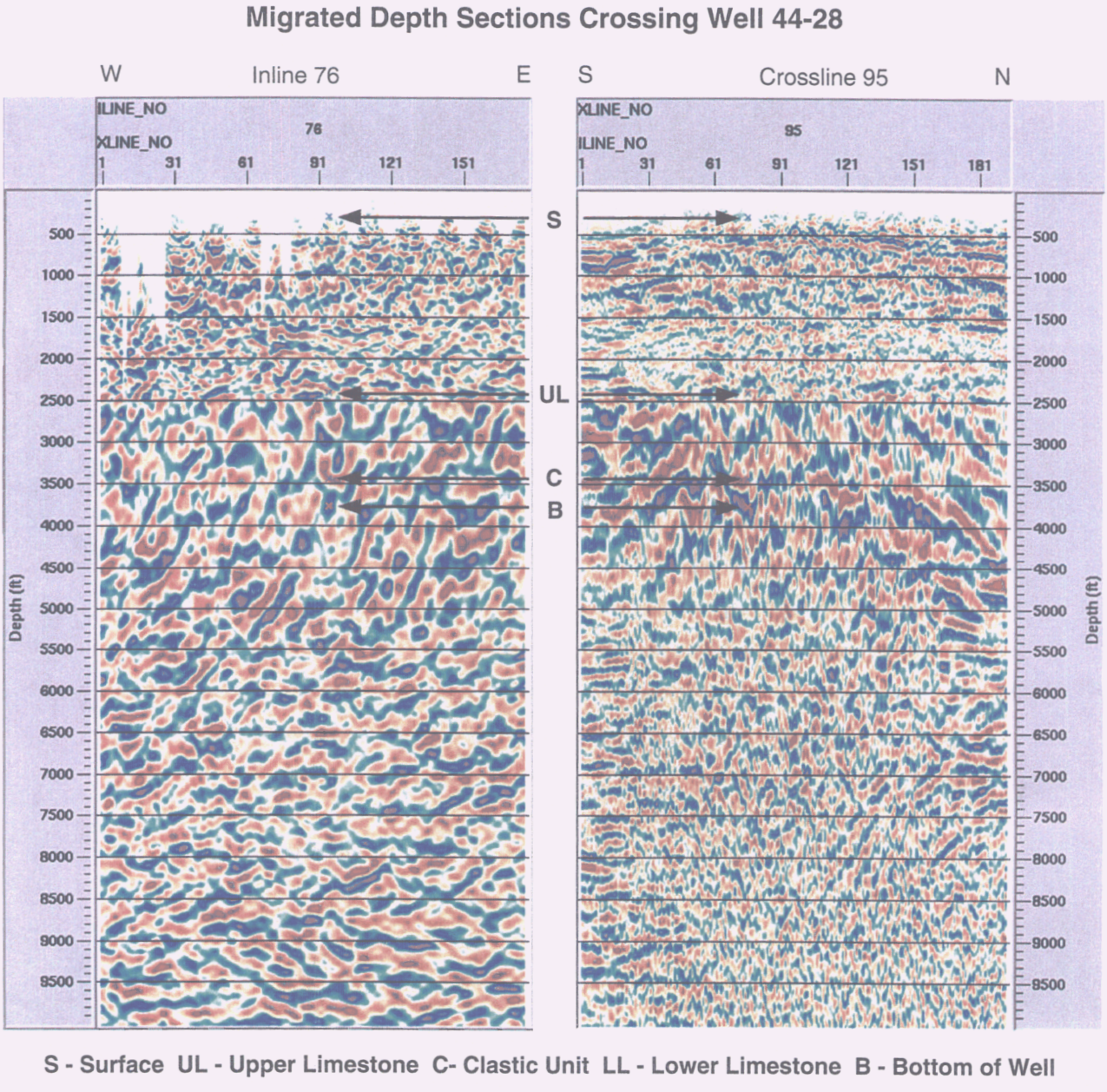

Figure 8b. Shown here are the two final migrated depth sections that cross the producing Well 44-28. The total depth of the well is marked along with important geologic contacts shown in Figure 3.

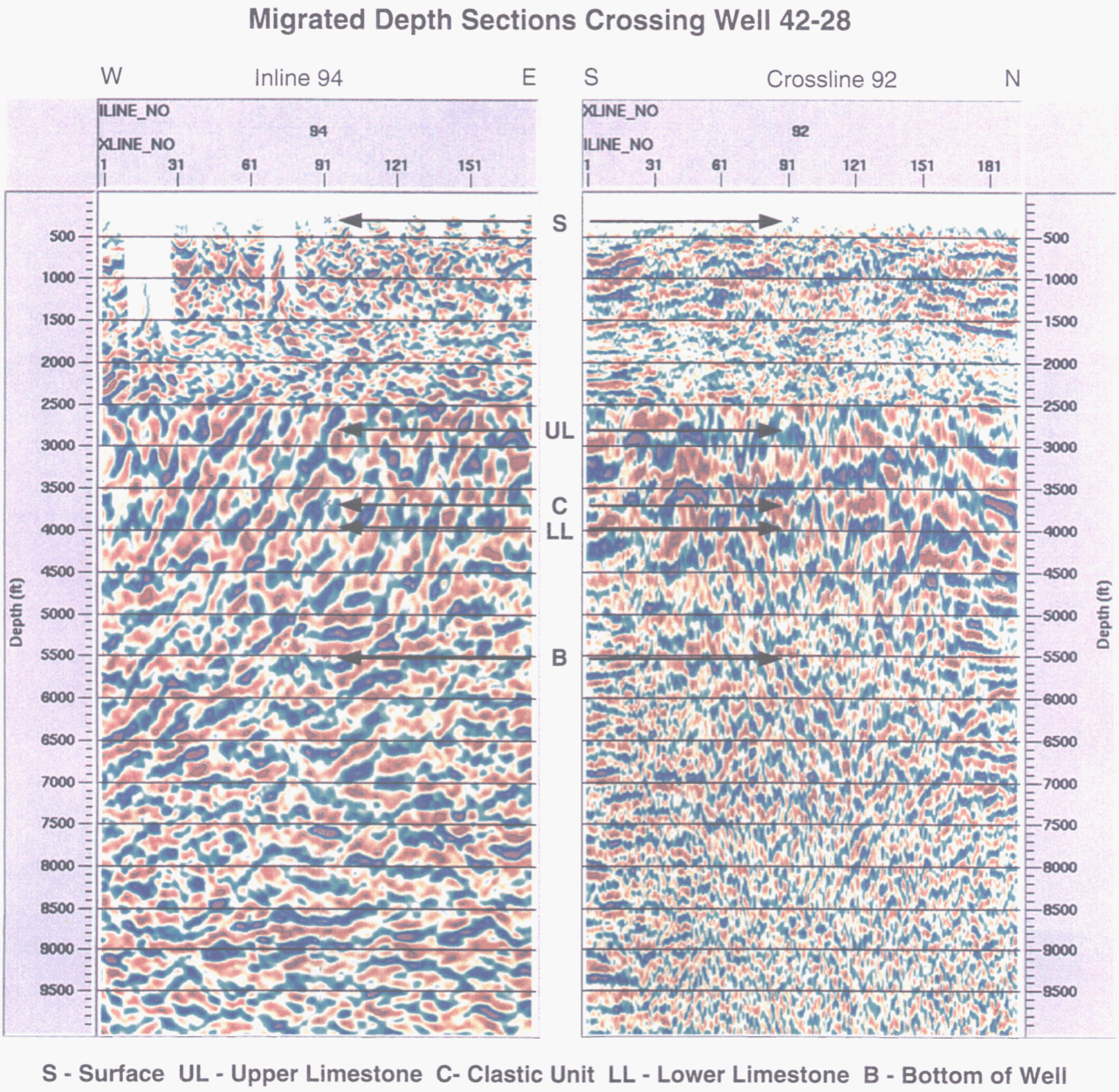

Figure 8c. Shown here are the two final migrated depth sections that cross the Well 42-28. The total depth of the well is marked along with important geologic contacts shown in Figure 3.

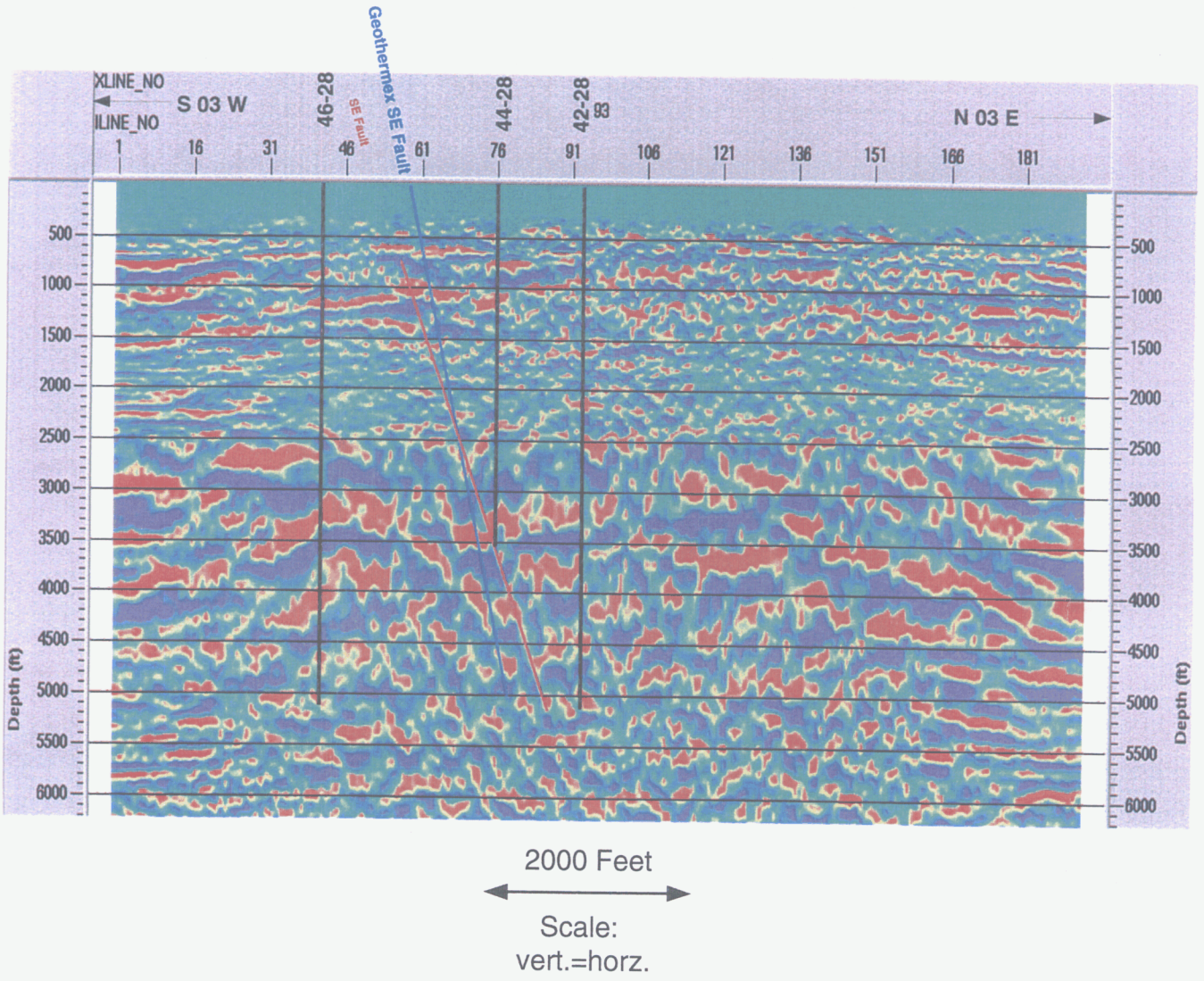

Figure 9. Final migrated depth section (crossline 93). The boreholes and the fault interpretations are superimposed for reference.

Example Results of Automatic Picking of First Breaks

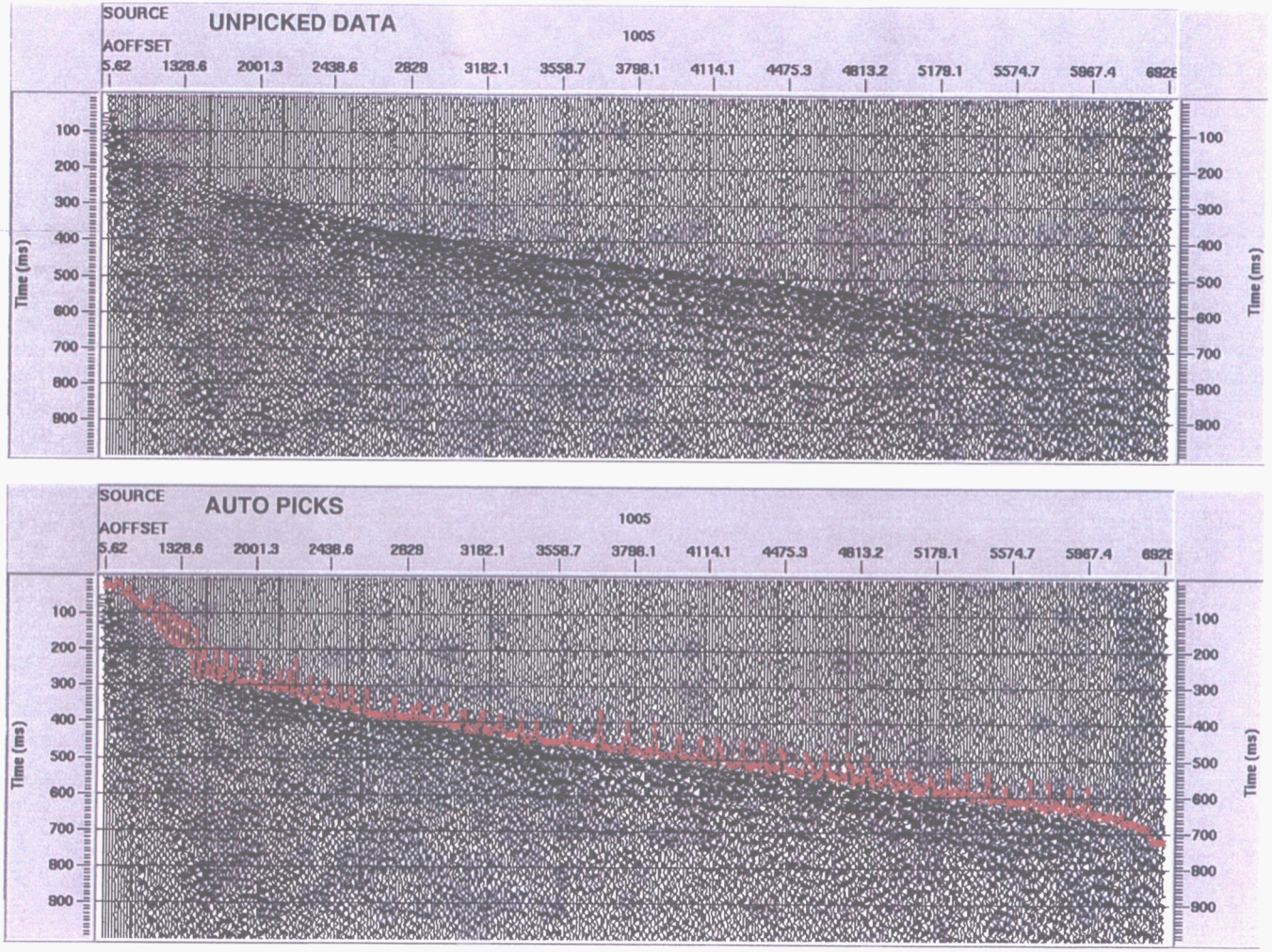

Figure 10. Example of first break picking using automatic routines from the ProMAX processing package. Notice weak first arrivals on the unpicked data at offsets less than 2000 feet(top) and the spread of the picks from the automatic picking (bottom).

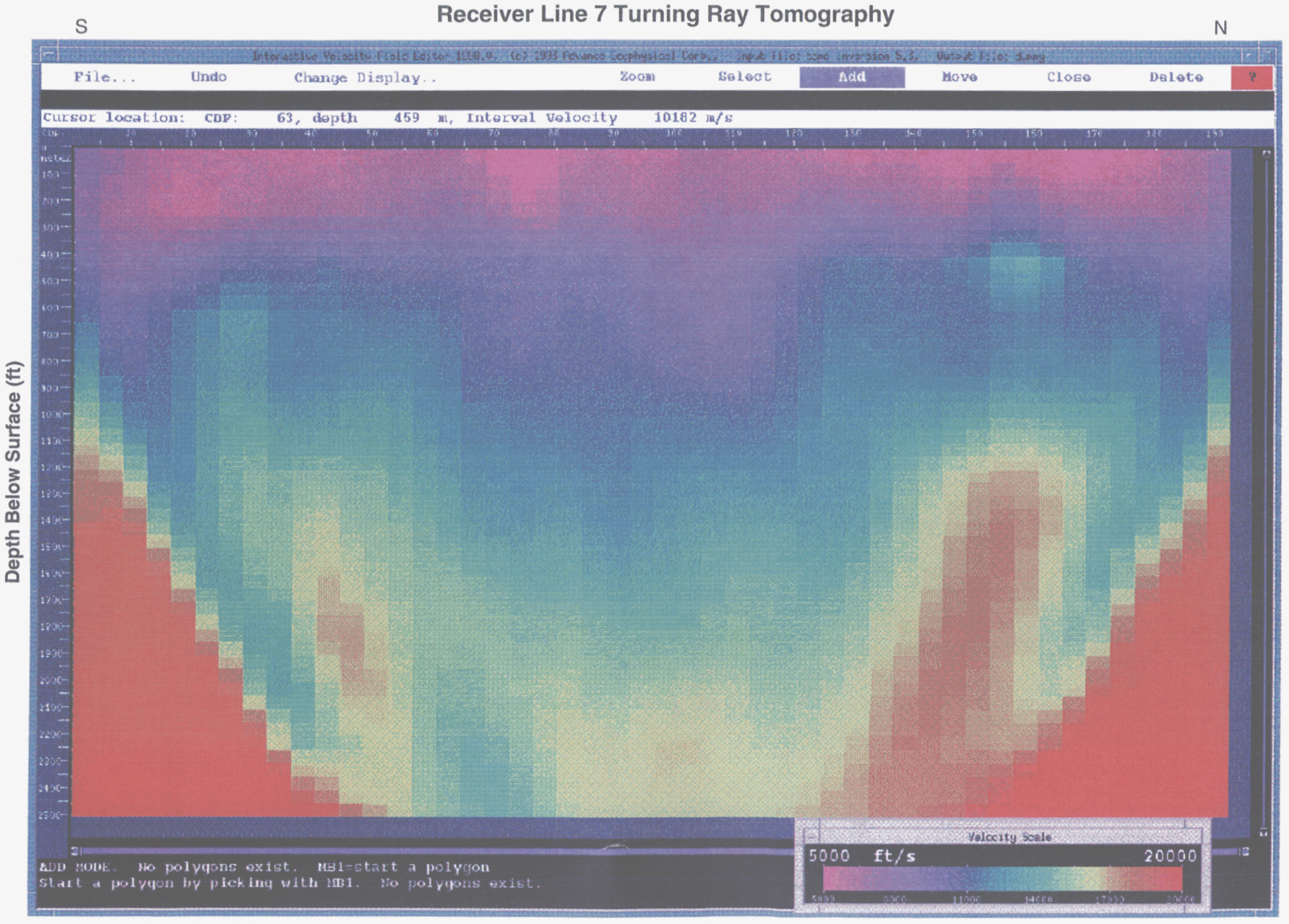

Figure 11. The results of turning ray tomography along receiver line 7.

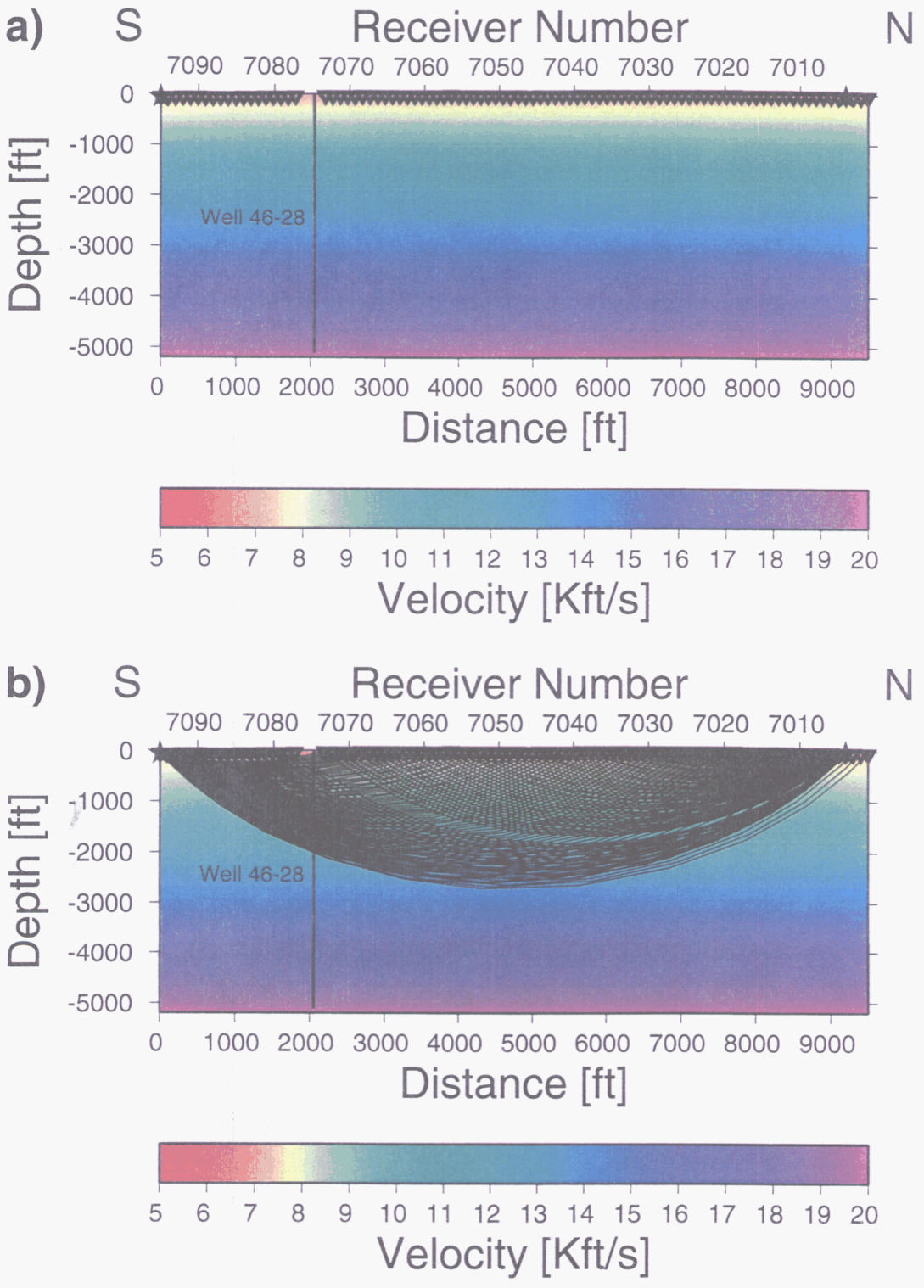

Figure 12. Starting velocity model for 2-dimensional ray tracing and travel time inversion. Receivers and sources are indicated by triangles and stars, respectively. The VSP well 46-28 is projected onto the image for reference.
a) Velocity model and source receiver geometry for 2 sources and 95 receivers along receiver line 7.
b) Example of an array of raypaths from 2 sources to all receivers along receiver line 7.

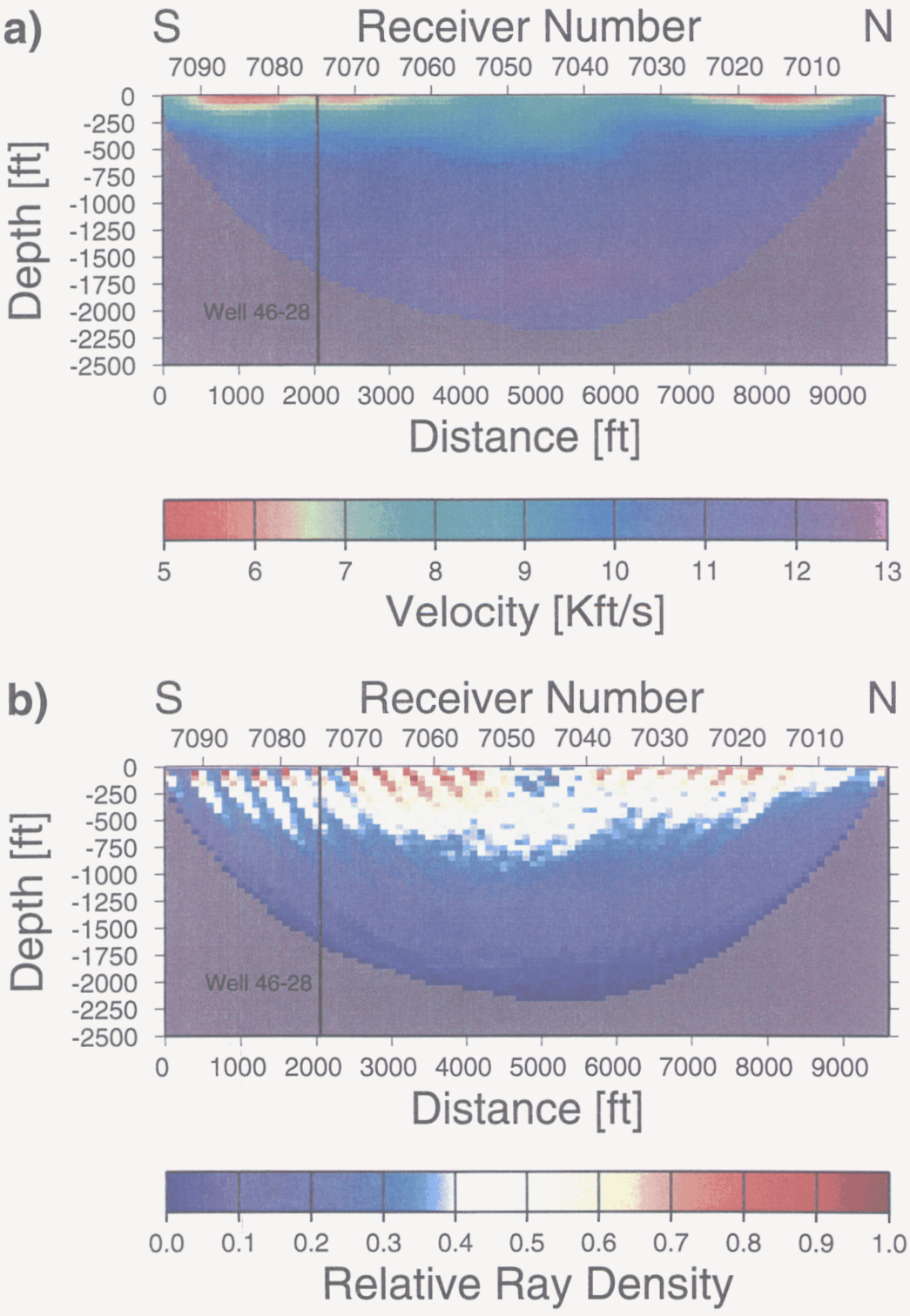

Figure 13. Travel time inversion results for receiver line 7. Gray areas represent no ray coverage. The VSP well 46-28 is projected onto the image for reference.
a) Velocity estimates.
b) Ray coverage (max number of rays per cell is 99).

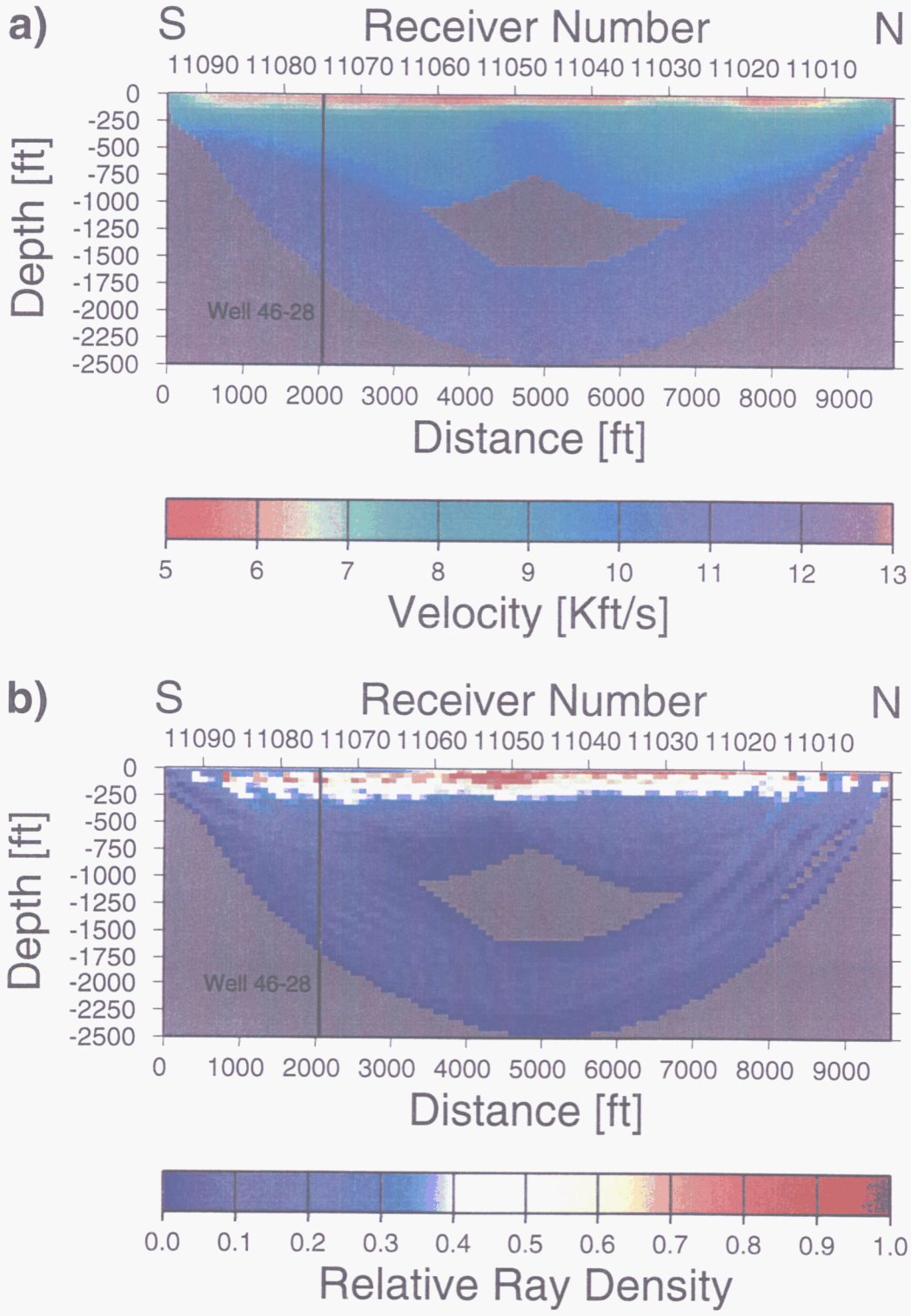

Figure 14. Travel time inversion results for receiver line 11. Gray areas represent no ray coverage. The VSP well 46-28 is projected onto the image for reference.
a) Velocity estimates.
b) Ray coverage (max number of rays per cell is 83).

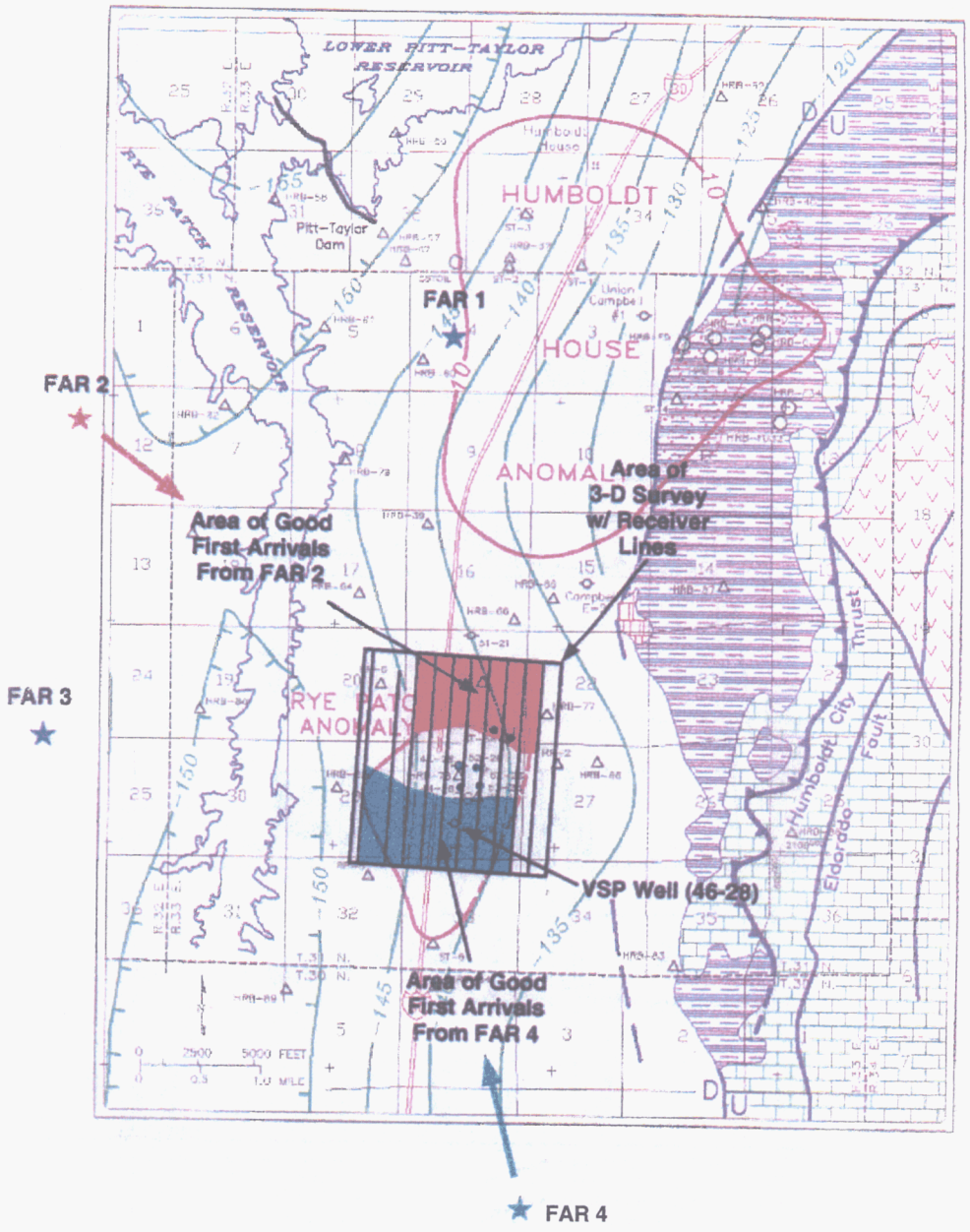

Figure 15. Location of four far-offset shots and areas where the receivers recorded a clear first arrival from Shots 2 (Northwest-orange) and 4 (South-green). Shots 1 and 3 had much weaker arrivals. The orange and green shaded areas represent distinct first arrivals for shot number 2 and 4, respectively. Beyond the boundaries of these areas the amplitudes of the respective first arrivals for shot number 2 and 4 become considerably weaker.

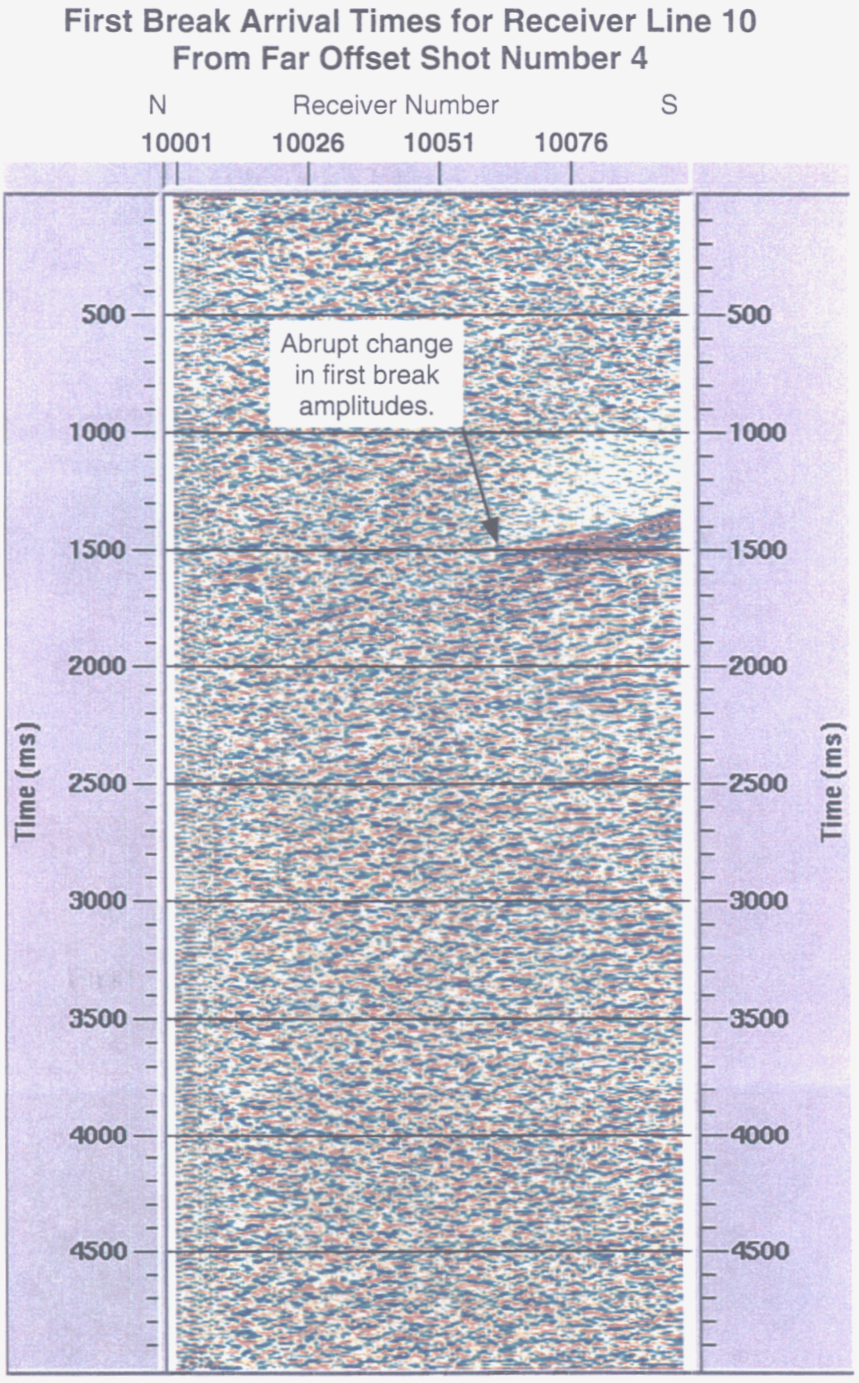

Figure 16. Abrupt change in the amplitude of the first breaks can be seen across Receiver Line 10 from Far-offset Shot Number 4.